An updated model providing long-term datasets of energetic electron precipitation, including zonal dependence

M. van de Kamp,[1] C. J. Rodger,[2] A. Seppälä,[2] M. A. Clilverd,[3] and P. T. Verronen[1]

Key points:

1. A previously published model for radiation belt energetic electron precipitation has been updated and improved.

2. The model includes dependences on: the geomagnetic index *Ap*, the *L* shell level relative to the plasmapause, and magnetic local time.

3. It provides the energy spectrum of 30–1000 keV precipitating electron flux for any period of time where the geomagnetic index *Ap* is supplied.

[1]Space and Earth Observation Centre,

Abstract.

In this study 30–1000 keV energetic electron precipitation (EEP) data from low Earth orbiting NOAA&MetOp Polar Orbiting Environmental Satellites (POES) were processed in two improved ways, compared to previous studies. Firstly, all noise-affected data were more carefully removed, to provide more realistic representations of low fluxes during geomagnetically quiet times. Secondly, the data were analyzed dependent on magnetic local time (MLT), which is an important factor affecting precipitation flux characteristics. We developed a refined zonally averaged EEP model, and a new model dependent on MLT, which both provide better modeling of low fluxes during quiet times. The models provide the EEP spectrum assuming a power-law gradient. Using the geomagnetic index *Ap* with a time resolution of 1 day, the spectral parameters are provided as functions of the *L*-shell value relative to the plasmapause. Results from the models compare well with EEP observations over the

Finnish Meteorological Institute, Helsinki, Finland.

[2]Department of Physics, University of Otago, Dunedin, New Zealand.

[3]British Antarctic Survey/NERC, Cambridge, UK.

period 1998–2012. Analysis of the MLT-dependent data finds that during magnetically quiet times, the EEP flux concentrates around local midnight. As disturbance levels increase, the flux increases at all MLT. During disturbed times, the flux is strongest in the dawn sector, and weakest in the late afternoon sector. The MLT-dependent model emulates this behaviour. The results of the models can be used to produce ionization rate datasets over any time period for which the geomagnetic *Ap* index is available (recorded or predicted). This ionization rate dataset will enable simulations of EEP impacts on the atmosphere and climate with realistic EEP variability.

1. Introduction

1.1. Particle precipitation modeling

There is currently considerable interest in the contribution of energetic particle precipitation (EPP) from the radiation belts into the atmosphere [*Matthes et al.*, 2017]. EPP provides an important source of odd hydrogen (HO_x) and odd nitrogen (NO_x) in the polar middle atmosphere [*Brasseur and Solomon*, 2005]. These in turn influence the polar ozone balance via several chemical reactions and catalytic reaction chains [e.g. *Randall et al.*, 1998; *Rozanov et al.*, 2012]. Furthermore, the initial polar middle atmosphere chemical changes are linked to dynamical variables in the stratosphere, propagating down to the troposphere and ground level [*Seppälä et al.*, 2009, 2013; *Arsenovic et al.*, 2016]. The impacts of these could be similar in magnitude to those arising from variations in solar spectral irradiance [e.g. *Rozanov et al.*, 2012; *Seppälä and Clilverd*, 2014; *Seppälä et al.*, 2014]. Thus, EPP can provide one of the pathways from the Sun into polar climate variability, and thereby provide essential input information for climate models.

Much work has been done to include the effect of proton deposition into atmospheric models [*Jackman et al.*, 2008, 2009; *Neal et al.*, 2013; *Nesse Tyssøy and Stadsnes*, 2015]. However, it has been found that the contribution of energetic electron precipitation (EEP) to EPP can be of similar importance in simulations of the polar winter stratosphere-mesosphere region [*Randall et al.*, 2015]. The relevant electron fluxes include those of low (auroral) energies (<30 keV), as well as those of medium and high energies (30 keV to several MeV).

In order to obtain EEP data as input to an atmospheric model dependent on location and time, direct satellite measurements are useful. However, when climate models are used to undertake long-term simulations of the influence of geomagnetic activity on the atmosphere, the input data need to describe the variability of the EEP forcing over many decades [*Matthes et al.*, 2017], extending beyond the timescales available from experimental satellite observations. The most useful long-term measurement of EEP is currently provided by the NOAA Polar Orbiting Environmental Satellites (POES) constellation, with several satellites at different Sun-synchronous polar orbits. These satellites carry the Space Environment Monitor-2 (SEM-2) instrument package [*Evans and Greer*, 2004; *Rodger et al.*, 2010a, b; *Yando et al.*, 2011], containing electron telescopes capable of measuring the medium energy electron fluxes (30 keV–2.5 MeV) that enter into the atmosphere. However, the time during which the SEM-2 instrument onboard POES has been providing a useful global coverage EEP dataset, spans less than two decades (from about 1998), and therefore a method of extending the time range of the EEP forcing data set is necessary.

In the absence of multi-decadal observations of energetic electron fluxes into the atmosphere, proxies that describe the overall impact of EPP on the atmosphere have been developed. These are often in the form of models which describe EEP patterns as functions of geomagnetic activity, based on statistical analysis of NOAA satellite observations [e.g. *Codrescu et al.*, 1997; *Wüest et al.*, 2005; *Wissing and Kallenrode*, 2009; *Whittaker et al.*, 2014a; *van de Kamp et al.*, 2016]. These models make use of the fact that the scattering processes which cause precipitation of medium- and high-energy electrons into the Earth's atmosphere are linked to the level of geomagnetic activity. Within the geomagnetic field energetic electrons are trapped, transported, and energized in the Van Allen Belts by processes such as radial diffusion and very low frequency (VLF) waves [*Thorne*, 2010]. During periods of high geomagnetic activity the fluxes of energetic electrons in the outer radiation belt can change rapidly by several orders of magnitude. Some of the flux variability is caused by the loss of electrons into the atmosphere at the footprint of the outer radiation belt, at high latitudes in both magnetic hemispheres.

In a previous paper [*van de Kamp et al.*, 2016], we used the POES SEM-2 measurements in concurrence with the geomagnetic indices *Dst* and *Ap* to derive proxies for the spectral parameters of the medium energy EEP flux. Here, we present two further upgrades of the *Ap*-dependent model. Firstly, we include better modeling of the low flux levels which occur during magnetically quiet times. Secondly, we present a version of the model with zonal dependence. These two points are explained further in the next two subsections.

1.2. Prediction of quiet-time fluxes

As noted above, measurements made by the SEM-2 experimental package onboard the POES satellites have been commonly used to study EEP. When considering the mesosphere, the EEP observations are provided by the Medium Energy Proton and Electron Detector (MEPED). Technical details of the MEPED detector are given by *Evans and Greer* [2004]. Some of the MEPED electron measurements have the advantage of being made inside the bounce loss cone (BLC) [*Rodger et al.*, 2010b, c], where the electrons are directly lost into the atmosphere, which is in itself comparatively unusual for radiation belt electron flux observations. MEPED/SEM-2 instruments have flown on multiple low-Earth orbiting satellites since 1998 and many of these are still operating at the time of writing. Thus there is a reasonably long set of measurements available, with simultaneous observations of EEP activity in different spatial locations and representing a wide range of different geophysical conditions.

However, the measurements are subject to several limitations, as outlined in Appendix A. One of these limitations is that the locally precipitating fluxes in the BLC are typically low, much lower than those in the drift loss cone (DLC), which have also been observed by various spacecraft, e.g. by DEMETER [*Sauvaud et al.*, 2006]. The fluxes in the BLC, particularly for relatively high electron energies, are often in the order of only a few hundreds of electrons/(cm^2 s sr) even during moderate geomagnetic disturbances. This corresponds in the MEPED observations to only a few single electrons per second in the detector aperture of 0.01 cm^2 sr [*Evans and Greer*, 2004]. Due to this, the MEPED electron flux measurements are comparatively insensitive, and suffer from (quantization and other) noise at a relatively high flux value (about 10^2 el./(cm^2 s sr)). Therefore, unless some care is taken, it may appear from the MEPED/POES electron fluxes that there is a constant background EEP flux at all times and all locations, although there is no experimental evidence to suggest these levels of constant EEP flux are truly happening.

The significance of this level of the noise floor of MEPED/POES causing "unreal" EEP fluxes was earlier considered by *Neal et al.* [2015] (section 6). They reported that the EEP fluxes at this noise floor level are sufficiently high to produce a 4 time increase in the noontime electron number density at around 75 km altitude. Such constant low-level EEP flux would also lead to a significant overestimation of NO$_x$ production during polar winter conditions, which is likely to influence the simulated effect on ozone, and hence the accuracy of dynamical coupling processes in climate modeling. The noise-floor EEP flux levels are likely to be dominant during geomagnetic quiet times, when there is little plasma wave activity to scatter radiation belt electrons into the atmosphere and hence produce EEP. The momentary absolute overestimation caused by this will not be large since the noise-floor flux levels are low, however these can lead to significant errors when integrating over long-term quiet periods in the climate models.

In the current study we improve the analysis of *van de Kamp et al.* [2016], to avoid the overestimation of precipitating electron fluxes during quiet times, by ignoring as much as possible any noise-affected measurements and making sure the fluxes at quiet times will be underestimated rather than overestimated.

1.3. Zonal dependence

There is considerable evidence, both from models and from observations, that energetic particle precipitation is not zonally uniform, but significantly dependent on magnetic local time (MLT). As there is considerable diurnal variation due to chemical cycles and solar illumination, the MLT dependence of the EEP forcing may well cause significant differences in the impact seen in a chemistry climate model.

There are many examples of EEP being MLT-dependent in the existing literature. For instance, *Hartz and Brice* [1967] showed from a collection of observations that discrete, 'burst-like' precipitation events show a peak in occurrence just before midnight, around 22 MLT, and more continuous precipitation events maximize in the late morning, around 8 MLT, while the combination of the two shows a more even distribution over the morning sector, and a minimum in the afternoon sector, between 12 and 18 MLT.

Parrot and Gaye [1994] found from wave observations up to 4.6 kHz by the GEOS 2 satellite at L value 6.6, that the most intense whistler-mode chorus wave emissions were between 6 and 9 local time (LT), and the least intense between 16 and 22 LT. They note that this minimum might be affected by the fact that the observation point tended to pass within the plasmasphere around 18 LT. However, the rest of their study shows that this is likely not the only reason for the duskside wave intensity minimum, for instance from the observation that the statistics for only disturbed conditions (when the plasmasphere should be so small that L=6.6 is well inside the radiation belt), show the same patterns.

Summers et al. [1998] explained, from theory and simulations, that whistler-mode chorus emissions can be excited by cyclotron resonance with anisotropic electrons between 22 and 09 MLT in the region exterior to the plasmapause. They summarized known theory and observations about the spatial distribution of various plasma waves, and displayed them clearly e.g. in Figure 7 of their paper. While their paper focuses upon the acceleration of radiation belt electrons, the plasma wave summary provides a useful overview of the variations in wave activity likely to drive EEP.

While these zonal patterns in radiation belt behavior have been known for some time, empirical models that quantify the dependence of EEP on MLT have not yet been developed. This is presumably due to the difficulty of making statistically significant observations of the zonal dependence: to gather statistically significant data dependent on L, MLT, and magnetic disturbance level, requires consistent observations made over a long enough time that for all values of these three variables, statistically significant numbers of data points are obtained. It seems likely that the POES/SEM-2 observations, which start from 1998 and have included multiple satellites, form the first ever dataset which comes close to meeting this requirement. This possibility has already been exploited by some researchers:

Wissing et al. [2008] compared MEPED BLC fluxes of POES satellites passing in different sectors, and found that those passing in the morning sector recorded significantly larger electron fluxes in the polar oval than those passing in the evening sector, both in geomagnetically quiet and disturbed conditions.

Meredith et al. [2011] found that precipitation of > 30 keV electrons during a high-speed solar wind stream was highest in the pre-noon sector, and for $L > 7$ also in late evening.

Whittaker et al. [2014a] divided the POES data in two MLT ranges with the aim to separate the data between two different forms of wave activity in the radiation belt: chorus waves between 01 and 08 MLT, and plasmaspheric hiss between 11 and 16 MLT. This demonstrated the significant changes in EEP magnitude when MLT is considered, even in a coarse manner.

Ødegaard et al. [2017] studied how BLC fluxes during storms increased compared to pre-storm time, and found for >30 keV and >100 keV the strongest increase in the pre-noon sector.

MLT-dependent analysis of POES fluxes has also been performed to study other phenomena than the one of this paper, e.g. *Horne et al.* [2009] focused on relativistic electron precipitation (>300 keV), which were found highest on the night side in their Figure 2f-h.

In this paper, the POES SEM-2 observations of medium-energy EEP inside the BLC are binned and analyzed with zonal dependence. The zonal dependent part of the data analysis will be explained in Section 2.3.

2. Reanalysis of POES/SEM electron flux measurement

This section describes the processing that was performed to the POES observation data in this new reanalysis. It also includes the processing parts that are the same as in the analysis of our previous paper; however, for a more complete discussion on the background considerations for this (e.g., of the spectral fitting), the reader is referred to *van de Kamp et al.* [2016].

2.1. Binning and noise removal

The current study makes use of the flux data measured inside the BLC over the years 1998–2012 by the POES SEM-2/MEPED instrument onboard the satellites NOAA-15, NOAA-16, NOAA-17, NOAA-18, and NOAA-19, as well as MetOp-02. During this time, the number of measuring satellites increased from one at the start and two from September 2000, to six at the end.

The SEM-2/MEPED instrument measures the electron flux in a part of the BLC. During disturbed times, when pitch angle diffusion is high, it can be assumed that this flux is representative for the average flux in the entire BLC, while this will be an underestimation during quiet times (see point 5 in Appendix A).

The detector monitors medium energy electron precipitation using three measurement channels. These provide the EEP electron fluxes in three different energy ranges: >30 keV, >100 keV and >300 keV. The nominal upper energy limit is 2.5 MeV for all three channels. In the current study, all available flux data in each of the three channels were binned dependent on: IGRF L-shell, at resolution of 0.2; time, at resolution of 1 hour; and MLT, at resolution of 3 hours. The data were integrated (averaged) over every bin.

Regarding the influence of the detector lower sensitivity limit and noise level of around 100 electrons/(cm^2 s sr) (see point 1 in Appendix A), it was considered that all measured samples which were near this level were to some extent affected by noise, and would affect the modeling for low fluxes if they were used. In order to avoid this influence, and with a wide safety margin, all samples (bin averages) where the flux in any of the three channels was below 250 electrons/(cm^2 s sr), were replaced by zeros in all three channels. This makes sure that all low-flux samples, whose true values are not known, are underestimated rather than overestimated.

However, it should be noted that although this measure removes the noise-affected samples, it also creates an artifact which can then affect the data analysis. Inevitably, the lowest flux observations tend to be at the high-energy channel >300 keV. Removing the samples with a low flux in any channel causes the samples with moderate integrated >30 keV fluxes and low >300 keV fluxes to be removed, while those with the same >30 keV flux but with higher >300 keV fluxes to remain. This can lead to an artificial flattening ('hardening') of the average spectrum when fluxes are near the cut-off level. We will account for this when fitting a model to the data, to make sure that impacts of this artifact do not influence the final EEP model.

Next, all flux data, including the zeros, were averaged over the hours of every day. In addition, for the zonal averaged data analysis, they were also averaged over all MLT zones. Note that this averaging means that the averages, which represent daily and globally integrated flux values, can have lower nonzero values than 250 electrons/(cm^2 s sr). Furthermore, given that the zero hourly values are known to be underestimations of low fluxes, this also means that the average values at the low end of the range (below about 250 electrons) are likely to be underestimations rather than overestimations, and are hence a conservative representation of the EEP flux.

2.2. Spectral fitting

From the three energy ranges measured by POES SEM-2 it is possible to fit an energy flux spectrum.

In an earlier measurement campaign, the DEMETER satellite measured the much higher fluxes of precipitating electrons in the drift loss cone at very high energy resolution [*Whittaker et al.*, 2013]. Differential spectral flux observations from these observations showed that a power-law relationship decreasing with energy is typically appropriate for precipitating electrons in the medium-energy range in the outer radiation belt [*Clilverd et al.*, 2010]. Therefore, as in the previous study [*van de Kamp et al.*, 2016], a power-law model for the spectral density S of the electron flux (i.e., the differential electron flux) is assumed:

$$S(E) = CE^k \qquad \text{electrons}/(\text{cm}^2 \text{ sr s keV}) \tag{1}$$

where E is the energy of the electrons (keV), C is an offset and k (≤ -1) is the spectral gradient. This spectral density can be integrated to obtain the integrated flux as measured between two energy levels. With these two energy levels described as the lower boundary E_L and the upper boundary E_U, the integral electron flux is given by:

$$\begin{aligned} F(E_L) &= \int_{E_L}^{E_U} S(E')dE' \qquad \text{electrons}/(\text{cm}^2 \text{ sr s}) \\ &= \begin{cases} \dfrac{C}{k+1}(E_U^{k+1} - E_L^{k+1}) & (k \neq -1) \\ C(ln(E_U) - ln(E_L)) & (k = -1). \end{cases} \end{aligned} \tag{2}$$

Here, the lower limit E_L is the annotated energy level of the channel (30, 100 or 300 keV), which will be denoted as E from this point on. For the upper cutoff E_U of the energy spectrum, 1000 keV was assumed, since it was found that above this energy the EEP flux spectrum typically deviates from a power law, and starts decreasing much more strongly [*van de Kamp et al.*, 2016].

Eq. (2) can be written as a function of F_{30} and k, where $F_{30} = F(30)$ is the flux >30 keV:

$$F(E) = \begin{cases} F_{30}\Big(\dfrac{1000^{k+1} - E^{k+1}}{1000^{k+1} - 30^{k+1}}\Big) & (k \neq -1) \\ F_{30}\Big(\dfrac{ln(1000) - ln(E)}{ln(1000) - ln(30)}\Big) & (k = -1). \end{cases} \quad (3)$$

The parameters F_{30} and k will be used to characterize the spectrum in this study.

The model of Eq. (3) was fitted to the zonally averaged data of the three integrated energy channels E, for each L (of resolution 0.2) and each day. The outputs of this procedure are the spectral gradient k and F_{30} for each day and each L.

To analyze the flux data dependent on magnetic activity, the data are classified according to the concurrent values of the magnetic index Ap. This index is the daily average of the three-hourly index ap, which in turn indicates the peak-to-peak variation of magnetic field strength (after subtraction of a quiet-time curve), measured over 3 hours, and weighted averaged over 13 geomagnetic observatories between 44° and 60° northern or southern geomagnetic latitude. As such it is a useful indicator of the geomagnetic effects of solar particle radiation (see http://isgi.unistra.fr/indices_kp.php). The unit of Ap is approximately equal to 2 nT.

The data of F_{30} and spectral gradient k were, for each L, binned dependent on Ap on a logarithmic scale. Next, the median value of F_{30} and k for each bin was calculated. The resulting medians for each bin of Ap and L are shown in Figure 1.

It should be noted that, since low flux values were replaced by zeros (see Section 2.1), some of the daily averages are zero, which led to zero values for F_{30} in Eq. (3). These zeros were all taken along in the calculation of the median F_{30} in the left-hand graph of Figure 1 (with some of these medians being zero themselves). However, from zero daily fluxes it was not possible to fit a value for k in Eq. (3). The median k shown in the right-hand graph of Figure 1 was therefore calculated only from k values obtained from nonzero daily average fluxes. Hence, the numbers of data in each bin for k is not necessarily the same as for F_{30}. In the bins where the portion of data samples for k was smaller than 25% of all data samples, the median values of k were considered not representative, and were excluded from the right-hand graph of Figure 1.

Figure 1 shows that for low Ap levels (typically <5) the magnitude of the electron precipitation fluxes are low at all L-shells. At high Ap values (typically >10) the observed fluxes are very low only at low L-shells. Peak fluxes of around 10^6 el./(cm^2 sr s) occur at decreasing L-shells as Ap increases, which is consistent with the expected inward movement of the plasmapause as geomagnetic activity is enhanced. For the highest Ap (>70), fluxes are enhanced over a wider range of L-shells than is seen at lower Ap ranges. Higher Ap levels correspond to greater geomagnetic disturbances, which are likely to involve multiple substorms. It has previously been shown that substorms lead to strong precipitation over a wide L-shell range [*Cresswell-Moorcock et al.*, 2013], which would explain the EEP enhancement seen in Figure 1 for those Ap conditions.

Typically where high fluxes occur, the power-law gradient is found to be roughly around -3.5. For low flux regions, i.e., at lower L and during lower Ap, the gradient slightly increases (as long as a spectral gradient calculation is possible). The steepest gradient values, below -4, occur at high L and moderate Ap, i.e., slightly offset from the region of very high flux. This can probably be explained assuming that there are different scattering drivers (different mixes of waves), with many varying parameters, causing diffusion in the radiation belt. These may cause the scatter rates to depend on magnetic activity in different ways at different energy levels, and hence cause the spectrum to change with Ap and L.

Clilverd et al. [2010] reported, from the high spectral resolution observations using DEMETER, individual observed spectral gradients between -1 and -3. Such values are also found here, although most gradients in Figure 1 are steeper. Note however that no statistical analysis of the spectral gradient was performed on the DEMETER data.

While the fluxes decrease gradually with L moving away from the middle of the radiation belt, at some Ap-values, the gradient can be seen to increase quite suddenly and irregularly with increasing or decreasing L (e.g. for $Ap > 40$ and $L > 8$). This sudden change in behavior is considered a consequence of the artificial flattening of the spectra for low fluxes due to the noise removal procedure, as explained in Section 2.1. As mentioned, this artifact will as much as possible be kept out of the model to be fitted to the data.

2.3. Zonal dependence

For the purpose of an analysis dependent on magnetic local time, we need a symbol for this parameter, which we will write as MLT, i.e. in italics. In this analysis, the measured fluxes in the three energy channels, measured over the years 1998-2012, were processed as described in Section 2.1, with the exception that the fluxes were averaged only over the hours of the day; the eight 3-hour MLT bins were kept separate.

The value of MLT used in the binning is taken from the POES data file. In the relevant data manual [*Evans and Greer*, 2004], the MLT definition is said to be calculated following *Cole* [1963] and *Fraser-Smith* [1987], as the magnetic longitude from the midnight magnetic meridian, converted to hours at 1 hour per 15 degrees.

The binning for separate MLTs introduced the risk of reducing the data density to critical levels, as explained by the following. Each satellite passes through an individual L-shell bin four times in each orbit, i.e., 3 passes per hour. For six satellites this represents 18 passes through an L-shell bin each hour. Over eight 3-hr MLT zones there are therefore only about 2 passes/zone/hour. Fortunately, this density reduction was compensated by the daily averaging as mentioned in Section 2.1, increasing it to 48 passes/zone/day.

The daily averaging also solves another problem. The observations are non-uniformly distributed in MLT due to the satellite orbital configurations [*Carson et al.*, 2013]. The daily averaging compensates this by spreading the samples evenly over the 3-hour zones, when enough satellites are operating. This is not entirely true only in the beginning of the measuring period, when just one satellite was measuring using a SEM-2 instrument. As a consequence, due to data sparsity, in the period January 1998 to September 2000, the data were somewhat unevenly spread over the MLT-bins. This point will be dealt with below.

The spectral fitting according to the model of Eq. (3) was applied also to this MLT-dependent dataset, resulting in a set of the flux parameters F_{30} and k, dependent on day, L, and MLT. Similarly as in the previous subsection, these data were subsequently binned dependent on concurrent value of Ap on a logarithmic scale. The median F_{30} and k of each $Ap/L/MLT$-bin are shown in Figures 2 and 3 as functions of Ap and L in eight 3-hr MLT panels.

When comparing these figures to Figure 1, it should be noted that these MLT-dependent data are of lower quality than the zonally averaged data, especially in the low flux range. This is because while the zonally averaged flux data were averages over 24 hours and 8 MLT zones, the MLT-dependent data set are averages over 24 hours only, i.e. over smaller groups of values, which leads inevitably to lower statistical significance. The median values for the Ap/L-bins reflect this effect, e.g. in the low flux range (low Ap, and low and high L). In both data sets, the flux values in this range are averages from groups of values which likely contain zeros (i.e. noise-affected values which were replaced by zeros), which can lead to relatively irregular results, but more so in this data set than in the zonally averaged data set. This explains the sharp edges near the zero-flux areas in Figure 2, while the equivalent areas in Figure 1 shows much smoother transitions.

In Figure 2, for low Ap (typically <5) the electron precipitation fluxes are very low at almost all L-shells and MLT; only in the midnight section ($21<MLT<03$), is some flux observed between L-shells 6 and 7. During moderate to disturbed conditions ($Ap>15$), the highest fluxes occur after dawn ($06<MLT<09$), and the least high fluxes before dusk ($15<MLT<18$). This pattern is in agreement with other reports mentioned before, of variations in chorus wave activity [*Parrot and Gaye*, 1994; *Summers et al.*, 1998] and in precipitation [*Hartz and Brice*, 1967; *Meredith et al.*, 2011; *Ødegaard et al.*, 2017].

In Figure 3, the variation of k with MLT is not as obvious as observed for F_{30}; the variation between the MLT-zones seems rather stochastic. Similarly as seen in Figure 1, the steepest gradient values, around -4, occur at high L and moderate Ap, i.e., slightly offset from the region of very high flux (c.f. Figure 2).

As mentioned above, the data were notably unevenly spread over the MLT-bins in the start of the measurement period up to September 2000. In particular, in the zone $12<MLT<15$, the data density was only about 65% of the average data density of all the zones. This unevenness could lead to a bias in the results of Figures 2 and 3, if that period would happen to show different statistical correlations between F_{30}, k, Ap, L, and MLT than the rest of the measurement period. In order to check this, the figures of this section were also produced using the data only from October 2000 onward (which contain no noticeable unevenness of data density over MLT). The results were not notably different from Figures 2 and 3, meaning that the inclusion of the period before October 2000 does not disrupt the statistical dependencies found. We therefore proceed with the analysis using observations covering the full measurement period 1998–2012.

In both Figures 2 and 3, it can be noted that the results for $Ap > 60$ are more irregular than for lower Ap. The main cause for this is the small number of data points for disturbed conditions. Due to the MLT binning, the numbers of data points in each bin is 8 times lower than for the MLT-independent results which were presented in Figure 1, and the number of data points for $Ap > 60$ falls below 10 points per bin in the MLT-dependent analysis. For such small numbers of data points, the medians can not be considered an accurate representation of the overall behavior. Furthermore, the observation from Figure 1 can also be noted in Figure 2: F_{30} for Ap>60 has high values over a wider range of L-shells than for Ap<60, which is likely to be the result of substorms.

In the model development described in the next section, all data points which are notably irregular as a result of any of the problems mentioned here, will be ignored when fitting curves to the data.

3. Formulation of the models

3.1. Model based on *Ap* and *L*

For the MLT-independent model, we used the globally averaged flux data described in Sections 2.1-2.2 and shown in Figure 1, i.e. averaged over all hours of each day and over all MLT zones.

To derive the model, the spectral parameters F_{30} and k resulting from the fits in Section 2.2 were binned depending on Ap and S_{pp}. Here S_{pp} is the distance to the plasmapause in terms of L, i.e.

$$S_{pp} = L - L_{pp} \tag{4}$$

where the location L_{pp} of the plasmapause is calculated according to the formula used previously [*van de Kamp et al.*, 2016]:

$$L_{pp}(t) = -0.7430 \; ln \; max_{t-1,t} \, Ap + 6.5257 \tag{5}$$

where $max_{t-1,t}\, Ap$ indicates the maximum value of Ap of the day of interest and the previous day. Equation (5) was derived from the plasmapause model by *O'Brien and Moldwin* [2003], by fitting coefficients to their relation given in Kp combined with the defined relationship between Kp and *ap*.

Subsequently, the model was derived by careful semi-automatic fitting to the median F_{30} and k, depending on S_{pp} and Ap. This was done as follows. For each dependence of one parameter on another, a choice was made from well-known mathematical functions (polynomials, power functions, exponentials, trigonometrics etc. and combinations thereof), to find a function that is able to reproduce the general behaviour seen from the data, taking into account criteria such as even accuracy in different parts of the range, and desired behaviour at high and low edges. The chosen function was then fitted by least-square error regression to the data points, to find its coefficients. Whenever the fit did not give a satisfactory result (as expressed in the mentioned criteria and error statistics as will be shown in Appendix B of this paper), it was discarded and the search for an optimal function was continued.

In addition to the function criteria mentioned above, another criterion in this process was that overestimation of low fluxes should be avoided as much as possible. This was done by noting, in the low flux range for either low Ap or low and high L, the values of F_{30} which show an irregular behavior with respect to Ap and S_{pp}, and not taking those values into account in the least-square error regression, but checking in the result that these values are underestimated by the functions rather than overestimated. If not, a different function was selected. For the gradient, the fitted curves were similarly made sure to underestimate irregular and relatively high values of k. Since in Section 2.2 it was noted that these irregular high gradients were affected by the artificial flattening of spectra due to the noise removal procedure described in Section 2.1, this way, that artifact is kept out of the model.

The resulting expressions for the model of the >30 keV flux, F_{30}, are:

$$F_{30} = \frac{e^{(15.004 - A)}}{e^{-5.5619(S_{pp} - 0.85072)} + e^{0.61055(S_{pp} - 0.85072)}} \qquad \text{electrons/cm}^2 \text{ sr s} \quad (6)$$

where

$$A = 19.683 Ap^{-0.66696}$$

Furthermore, $F_{30} = 0$ in all following cases:

- $Ap = 0$
- $S_{pp} < -0.3$
- F_{30} (according to Eq. (6)) < 10 electrons/cm^2 sr s.

The expressions for the model of the spectral gradient k are:

$$k = \frac{-1}{Acosh\Big(0.31955(Spp - s)\Big)} - 1 \qquad (7)$$

where

$$A = 0.30180 + 2.0821Ap^{-1.7235}$$

$$s = ln\Big(11.970 + 2.4824Ap^{0.7430}\Big)$$

In order to compare the model results with the zonally averaged POES observations, the values of F_{30} and k were calculated from Ap using the expressions above over the same time period and the same L values as the POES database. The results were binned as functions of Ap, and median values were calculated for every bin to allow direct comparison with Figure 1. The result is shown in Figure 4 in the same format as the POES observations shown in Figure 1. In the right-hand graph, the modeled gradient is not shown for bins where the modeled F_{30} is zero, since the gradient is meaningless for a zero flux.

Comparisons between this model and the measurements wil be given in Section 3.3 and Appendix B.

3.2. *MLT*-dependent model

To derive the MLT-dependent model, we used the spectral parameters F_{30} and k resulting from the spectral fits on the MLT-dependent data, as mentioned in Section 2.3. These spectral parameters were binned for Ap and S_{pp}, for the different MLT bins separately. Subsequently, the model was derived by careful fitting to the median F_{30} and k values depending on S_{pp}, Ap and MLT, using the same procedure and criteria as described in the previous section.

While fitting the model in equivalent formulas as Eqs. 6 and 7, it was noted that the variation of the data with S_{pp} did not depend noticeably on MLT. Because of this, and keeping in mind that the MLT-dependent data set is of lower statistical significance than the zonally averaged dataset, it was assumed that the dependence on S_{pp} can be assessed more accurately from the zonally averaged data set, especially considering that this part of the formula describes the behavior at the low/high-L flanks of the flux bulge, where fluxes are low and these data are relatively inaccurate. Therefore, the S_{pp}-dependent parts of the formulas in Eqs. 6 and 7 were assumed to be valid also for the MLT-dependent model. These parts were fixed in the procedure to fit the rest of the expressions for F_{30} and k as functions of Ap and MLT.

The resulting expressions for the model of the >30 keV flux, F_{30}, are:

$$F_{30} = e^{T} \frac{e^{-A} + e^{-B}}{e^{-5.5619(S_{pp} - 0.85072)} + e^{0.61055(S_{pp} - 0.85072)}} \text{ electrons/cm}^2\text{sr s} \quad (8)$$

where

$$T = 12.897 + 1.5047 sin\Big(MLT\frac{\pi}{12} - 0.87102 sin(MLT\frac{\pi}{12})\Big)$$

$$A = (0.039284Ap)^{-1.3203}$$

$$B = (0.037950Ap)^{H}$$

$$H = -0.98550 + 0.14235 cos\Big(MLT\frac{\pi}{12}\Big)$$

Furthermore, $F_{30} = 0$ in all following cases:

- $Ap = 0$
- $S_{pp} < -0.3$
- F_{30} (according to Eq. (8)) < 10 electrons/cm^2 sr s.

The expressions for the model of the spectral gradient k are:

$$k = \frac{-1}{Acosh\Big(0.31955(S_{pp} - s)\Big)} - 1 \tag{9}$$

where

$$A = 0.28321 + 1.1504 Ap^{P}$$

$$P = -1.0927 + 0.21415 cos\Big((MLT + 5.8983)\frac{\pi}{12}\Big)$$

$$s = ln\Big(11.970 + 2.4824 Ap^{0.7430}\Big)$$

In order to compare the model results with the MLT-dependent POES data, the F_{30} and k were calculated from Ap using the expressions above over the same time period and the same L and MLT values as the POES database. The results were binned as functions of Ap, and median values were calculated for every bin to allow comparison with Figures 2 and 3. The result is shown in Figures 5 and 6. The model shows the significant features dependent on MLT as found from the observed fluxes, with highest fluxes during $6<MLT<9$, and lowest fluxes during $15<MLT<18$, and EEP during low Ap conditions concentrating in the MLT range around midnight. While the model follows the observations well for high fluxes, it may be noted that the agreement is less good for low fluxes. This is because, as mentioned above, the low flux values of this MLT-dependent dataset were more irregular and considered less accurate than those of the zonal averaged data set, due to the lower statistical significance. Therefore the model was not aimed at following these low flux values too exactly.

As mentioned above, the significant feature in the MLT-dependence of the flux spectrum is the variation of the overall flux intensity with MLT. This is represented in Eq. (8) by the expressions for A, T, B and H. To show this variation more clearly, the corresponding part of the observed data is shown in the left-hand graph of Figure 7: the flux

F_{30} which is observed for $L = L_{pp} + s$, i.e. at the L-value where it tends to be highest, as a function of Ap and MLT. In the right-hand graph, the part of the model which predicts the same peak flux is shown: $e^T(e^{-A} + e^{-B})/2$, with T, A and B from Eq. (8).

The left-hand graph shows that in quiet conditions (Ap roughly below 10), the significant flux concentrates on the night side. When Ap increases, the flux intensifies at all MLT. However, it increases most in the morning sector ($6<MLT<9$), and it always remains lowest in the afternoon sector ($15<MLT<18$). In the right-hand graph, the model is seen to emulate this experimentally observed behavior.

Another interesting feature of the observed flux is that it tends to approach plateau levels at high disturbance values. This can be noted in Figure 7, mostly in the sector $6<MLT<9$: the flux does not significantly increase further when Ap increases above 50. In all other MLT sectors, such a saturation level was found to be approached as well, though more slowly.

Because of this observed behavior, a saturation level was implemented in both models, MLT-independent and -dependent: the modeled flux goes asymptotically to a maximum when Ap increases to high values. This can be seen in Eq. (6) and (8). In Eq. (6) when Ap goes to infinity, A approaches 0, so the modeled F_{30} will always stay below $exp(15.004)/2 = 1.6411 \times 10^6$ electrons/cm^{2}sr s, even if the disturbance would increase beyond the levels found in this study. In Eq. (8), when Ap goes to infinity, the maximum F_{30} approaches $exp(T)$. This value varies with MLT, between 8.8637×10^4 and 1.7971×10^6 electrons/cm^{2}sr s.

For the gradients, a similar saturation feature was found from the observations and implemented in the models. In Eq. (7), A approaches 0.30180 when Ap goes to infinity, so that the modeled k always stays above $-(1/0.30180) - 1 = -4.3135$. And in Eq. (9), A approaches 0.28321 when Ap goes to infinity, so that the MLT-dependent modeled k always stays above -4.5309.

It has also been verified that the MLT-dependent model and the MLT-independent model are consistent with each other. For this purpose, the results of the MLT-dependent model were zonally averaged, as follows: The F_{30} and k which had been calculated from Ap, L and MLT using this model, were used to calculate the three integrated fluxes >30 keV, >100 keV, and >300 keV (equivalent to the measured fluxes). Next, these modeled fluxes were averaged over all MLT zones, and these zonally averaged fluxes were used to fit the spectral parameters F_{30} and k as in Eq. (3). These spectral parameters were then compared to those from the MLT-independent model. It was found that the results were very similar: the relative difference between the two models in F_{30} was at most a factor 1.4 and mostly much smaller, and the difference in k was at most 0.17 and mostly much smaller.

3.3. Time-series comparison with POES measurements

As an example, the upper two rows of Figure 8 show plots of some time series of the measured > 30 keV (blue +) and > 300 keV fluxes (red *), as well as the predicted flux according to the MLT-dependent model (lines), for two selected L shells, time periods and MLT ranges. The left-hand graphs are for an active month, while the right-hand graphs represent a quiet month. The two MLT ranges chosen ($6<MLT<9$, upper row, and $18<MLT<21$, second row) generally have high flux and low flux magnitude, respectively. The third row of the figure shows the zonally averaged data, and the flux predicted by the MLT-independent model. The bottom row shows the Ap index for the respective periods.

It can be seen that the MLT-dependent model follows the measured flux quite well, although there remains a stochastic variation for individual days. The difference between the two MLT zones is generally well predicted. In the quiet month, the > 300 keV flux was so low that many data points were below the cut-off threshold. The zonally averaged fluxes are, as expected, in-between the ones for the two MLT zones. Also the MLT-independent model predicts values in-between the higher and lower ones predicted by the MLT-dependent model.

It may be noted that the MLT-dependent data show more fluctuations from day to day than the zonally averaged data. This is due to the fact that these data have been averaged less and are therefore more stochastic, as explained in Section 2.3. This also causes the difference between the MLT-dependent model and the respective measurements to be more variable than those for the MLT-independent model.

An example of the saturation of the flux, as explained in the previous section, can be seen here: on 29-30 March 2003, Ap reached high values, while the measured fluxes did not exhibit similar a peak on those days. A similar behavior was found in other events. This is why the models were made to emulate this behavior and ignore extreme values of Ap by means of the saturation.

These curves are just for illustration. The prediction accuracy of both models is assessed quantitatively, and more generally, in Appendix B. There, it is found that for the MLT-independent model, the median error of log_{10} of the > 30 keV flux is consistently within ± 0.2, and the median error of log_{10} of the > 300 keV flux is within ± 0.5. Both of these errors have standard deviations of mostly around 1.0, and up to 1.4 for the lowest fluxes. The MLT-dependent model has similar errors as the MLT-independent model when fluxes are large, while for lower fluxes the error can not be well assessed due to the fact that the MLT-dependent data are considered not statistically significant enough there.

A comparison of the MLT-independent model with the model previously published [*van de Kamp et al.*, 2016] is given in Appendix C. There it is shown that the two models give very similar results during disturbed conditions, but for $Ap < 10$, the MLT-independent model gives lower values than the previous model; this difference increases with decreasing fluxes.

4. Atmospheric Ionization Rates

This section shows how the flux spectra as presented in the previous sections correspond to atmospheric ionization rates caused by this flux.

For this purpose, the ionization rates for different altitudes were calculated over the entire measurement period of the data set used in this study. This was done, similarly as in the previous paper [*van de Kamp et al.*, 2016], by reconstructing the spectra of precipitation flux between energies of 30 and 1000 keV from the POES-observed spectral flux parameters F_{30} and k presented in Section 2.2, and entering these spectra as inputs to the parameterization of electron impact ionization derived by *Fang et al.* [2010]. This ionization rate calculation required a representation of the atmosphere, which was created using the NRLMSISE-00 model [*Picone et al.*, 2002]. This way, the ionization rates were calculated for each value of L and MLT, in profiles for altitudes from 23 to 140 km, and for every day of the measurement period.

The same calculation was also performed using the spectral flux parameters resulting from both presented models of this paper, for all the same L-shells and MLT values, and for every day of the period 1998–2012, with Ap as input.

In the following, the ionization rates thus calculated from the observed and modeled electron fluxes will be referred to as 'observed ionization' and 'modeled ionization' respectively (even though obviously no ionization rates were directly observed or modeled).

For presentation in the next figure, all observed and modeled ionization rate profiles, calculated from the zonally averaged data and the MLT-independent model, were binned as a function of Ap, similarly as in most graphs of this paper. Next, for each bin of Ap and L, the median ionization is shown in Figure 9. The top left panel shows the resulting median observed ionization at altitude h = 90 km as a function of Ap and L. Since 90 km is approximately the main ionization height of the lower-energy electrons of 30 keV, which have the highest flux spectral density in this energy range, this ionization level corresponds roughly to the observed flux of $>$ 30 keV electrons. Consequently the figure looks very similar to Figure 1 (left).

The top right panel of Figure 9 shows the median observed ionization for L=5.1 as a function of h and Ap. As was already shown in the previous paper [*van de Kamp et al.*, 2016], this figure indicates that the main part of the ionization due to the energy range considered in this paper (30-1000 keV) is between 70 and 110 km altitude, while the rates decrease rapidly at altitudes below and above. The occurrence of a peak of the ionization at about 90 km is caused partly by the 30 keV lower limit of electron spectrum energy. The lower altitude limit of the ionization of this energy range is seen at about 55 km, because the electrons with highest spectrum energy (1000 keV) can penetrate down to this height [e.g. *Turunen et al.*, 2009, Figure 3].

It should be noted that the ionization profiles due to electrons of energies below 30 keV and above 1 MeV will overlap the profile shown here, and show maximum ionizations at higher and lower altitudes, respectively. The altitude range which is dominated by ionization from electrons in the energy range considered in this study, and where the profile of Figure 9 can therefore be assumed to be close to the total ionization profile, is between about 60 and 95 km.

Interestingly, for Ap above about 30, the ionization appears almost constant with respect to Ap. This is due to the combination of the overall increasing flux and the simultaneous erosion of the plasmasphere as disturbance level increases, the latter causing the L shell of 5.1 to be more and more distant from the plasmapause.

The lower row of Figure 9 shows the corresponding median modeled ionization rates, as predicted by the MLT-independent model for the same median samples as in the top two graphs, as functions of h, L and Ap. Generally, the discrepancy between the median modeled and measured values is less than a factor 3. For an error analysis, the reader is referred to Appendix B, which analyses the modeling errors of the fluxes at different energies, which correspond to modeling errors of ionization at different altitudes.

In order to save space, a similar comparison between the MLT-dependent observed and modeled ionization is not shown, as this would require graphs as functions of L, h, Ap, and MLT; besides, these would not reveal any information which is not apparent in the comparison in terms of flux in Section 3.2 and Appendix B.

In the following, a few example cases of ionization profiles are shown.

Figure 10 shows the observed zonally averaged ionization profiles (stars) of three selected days and L-shell values. The three values of L and Ap of these example cases are written in the graphs, and are also indicated in the left-hand graph of Figure 1, which helps to identify the kind of precipitation which is shown here. The modeled ionization profiles (MLT-independent model) on these days at these L-values are also included (green lines).

Figure 1 shows that the left-hand panel of Figure 10 corresponds to low flux just outside the plasmapause in quiet conditions. The middle panel shows a case of strong flux at high disturbance, in the middle of the radiation belt. The right-hand panel shows a case of moderate flux and ionization, in the outer region of the radiation belt.

The ionization profiles for the same three example cases are shown as functions of MLT in Figure 11, as modeled by the MLT-dependent model. These show the amount of variation of ionization with MLT that can be expected if the MLT-dependent model is implemented. The same variations as seen in the flux in e.g. Figure 7 are seen here: at quiet times, the ionization is strongest around local midnight, and during moderate to disturbed times, it is strongest in the local late morning and lowest in the afternoon. The MLT-dependent pattern does not change much with altitude. This is due to the fact that k does not depend very much on MLT, as seen in Figures 3 and 6.

5. Conclusions

EEP fluxes, measured inside the BLC by the POES SEM-2 instruments throughout the period 1998–2012, have been processed in an improved way compared to earlier studies. Firstly, noise-affected low-flux data have been removed more thoroughly than before, which allows better isolation of the truly measured values from the noise. Secondly, the data have been processed statistically for 8 different MLT zones separately. This allows an analysis of the data dependent on MLT, which gives a clearer overview of the combined dependences of EEP on MLT, L-shell, and disturbance level.

It has been found that the EEP flux depends significantly on MLT. During quiet times, any measurable flux is only observed near midnight. As disturbance levels increase, the flux increases at all MLT. At disturbed times, the flux is strongest in the dawn sector, and weakest in the late afternoon sector. These observations are in agreement with previous observations by other researchers.

The improved data processing enabled the development of two models for radiation belt medium-energy (30-1000 keV) EEP flux, providing upgrades to the model published earlier [*van de Kamp et al.*, 2016]. Both upgraded models are improvements to the earlier model in terms of a more careful modeling of the low fluxes during quiet times. The behavior of these low fluxes is extrapolated downward from the behavior at higher fluxes, and therefore avoid not only the effects of the measurement noise floor, but also any artifacts caused by removing the noise-affected data.

One of the two models makes use of the MLT-dependent data processing, by including the dependence of MLT in the formulas. The model emulates the MLT-dependent behavior as found from the observations.

Both models use the magnetic index Ap as their only time-dependent input, and can therefore be used to generate a long-term dataset of the medium-energy EEP flux, and the resulting atmospheric ionization profile, for any period of time for which Ap is available, be it recorded or predicted. For the past, this can stretch from 1932 to the present. The validity of the models has been demonstrated between 1998 and 2012, for eight 3-hour MLT zones, for $1<Ap<100$, $2<L<10$, and a time resolution of 1 day.

The models were based on a data set with relatively few days with strong disturbance ($Ap > 60$). Future measurement campaigns during more disturbed conditions may allow to validate these models, and possibly extend the validity range in Ap upward.

The main impact of the ionization from EEP is focused on the mesosphere-lower thermosphere altitudes (70-110 km), with the lower limit of the ionization of this energy range located at about 55 km altitude. In future work, we hope to include additional precipitation mechanisms, for example expanding to relativistic energies >1 MeV. This would extend the range of impact altitudes, and bring us closer to being able to estimate the total impact of EEP forcing on the atmosphere.

Furthermore, future advances in this style of modeling might build on any advances addressing the limitations of the POES EEP flux observations, as described in Appendix A.

Appendix A: limitations of the POES EEP observations

The EEP representation described in the current study is based on the analysis of a long set of POES-provided EEP observations. While we believe this is the best set of EEP measurements currently available, it is important to acknowledge that the MEPED/SEM-2 instruments suffer from multiple issues which can lead to significant uncertainties in the EEP values. It is possible that in the future new approaches will be developed to compensate for some of these issues, which would then allow improvements in the EEP representation presented in the current study. We detail a number of known issues below.

1. MEPED/SEM-2 Electron Noise floor. As discussed in the current study, the MEPED/SEM-2 Electron Flux observations are strongly impacted by the noise floor of this instrument. This "floor" corresponds to a minimum measurement of one count per

second (in a 1 s period, measured every 2 s). As the smallest practical values the instrument can report are zero or one, it seems very difficult to see how this limitation can be corrected using the current instrument.

2. Low-Energy Proton Contamination. It has long been recognized that the MEPED/SEM-2 electron observations suffer from contamination due to protons in the 10s-100s keV energy range [*Evans and Greer*, 2004]. The significance of this contamination has previously been examined [*Rodger et al.*, 2010a; *Yando et al.*, 2011]. In practice, this means that the electron EEP fluxes can be significantly larger when there are large fluxes of relatively low energy protons present. In the current study, we have made use of the algorithm presented in Appendix A of *Lam et al.* [2010] to remove the impact of these contaminating protons. We note that this approach has been previously validated by *Whittaker et al.* [2014a], who compared POES EEP observations (both contaminated and corrected), against DEMETER electron fluxes.

We note that other authors have presented different approaches for this correction, for example *Peck et al.* [2015]. It is also worth noting that the proton measurements may suffer from degeneration due to long term radiation damage [e.g. *Asikainen and Mursula*, 2013]. This is an additional factor which could influence the proton correction, and hence the electron flux observations.

3. Solar Proton Contamination. Monte Carlo modeling of the MEPED/SEM-2 instrument indicates the electron flux observations will be very strongly impacted by the high energy protons present in the polar cap during solar proton events. Case studies show that the MEPED/SEM-2 electron observations are identical to the high-energy proton observations in this region during these times. We do not believe that any approach has

been developed to correct for this extremely strong contamination source. In our data processing the electron fluxes are removed during all solar proton events.

4. Spectral Fitting and MEPED/SEM-2 Electron Energy Ranges. The MEPED/SEM-2 instruments have only 3 channels of integral flux (>30 keV, >100 keV and >300 keV). Unfortunately, this energy resolution is much lower than one would like. In our EEP representation, we have used the 3 integral flux measurements, plus the assumption of a power law distribution (following the findings of *Whittaker et al.* [2013]), to produce spectral indices to describe the energy dependence of the EEP from 30 keV-1 MeV. A consequence of the rather low energy resolution is the difficulty in assessing the goodness of fit of the spectrum and hence the uncertainty of individual flux measurements. This affects most the lowest and therefore most noise-affected high-energy fluxes, and consequently the ionization rates at lowest altitudes.

5. Orientation and Geometry of the MEPED Detectors. In this study, we are using the measurements of the MEPED/SEM-2 telescope which is oriented vertically upward (also referred to as 'the 0° telescope') with a field of view of 30° wide [*Evans and Greer*, 2004]. For most geomagnetic latitudes (i.e., $L > 1.4$), this telescope measures inside the BLC [*Rodger et al.*, 2010a, b]. However, the size of the detector means it only views a small fraction of the BLC, and the pitch angle range observed inside the BLC is location dependent, as discussed by *Rodger et al.* [2013]. That study contrasted ground-based ionospheric absorption observations during POES overpasses and concluded that during low EEP periods, POES could significant underestimate the 'true' EEP flux, consistent with *Hargreaves et al.* [2010]. In contrast, during more disturbed periods, when strong diffusion scattering process dominate, *Rodger et al.* [2013] concluded that the POES EEP

fluxes were largely accurate. That conclusion has been supported by contrasting POES EEP with multiple years of subionospheric VLF EEP magnitude estimates [*Neal et al.*, 2015].

It is likely that the most important EEP forcing of the atmosphere is during the disturbed periods when high EEP levels dominate, and the POES fluxes are more accurate. However, it is possible that long-lasting small to moderate EEP fluxes could be significant to atmospheric chemistry, and that these much smaller EEP levels could be poorly detected by POES. Techniques are being developed to attempt corrections for this [e.g. *Nesse Tyssøy et al.*, 2016], and show much promise.

Appendix B: Error assessment

This Appendix demonstrates the performance of both models presented in this paper using an error analysis.

The error of either model in the >30 keV precipitating electron flux can be calculated as:

$$\epsilon_{F30} = log_{10} F_{30_{model}} - log_{10} F_{30_{POES}} \tag{B1}$$

First for the MLT-independent model, ϵ_{F30} has been calculated for every day of the data set and every L-shell value of the classification used in Section 2. The results of this were binned dependent on Ap, and subsequently statistically analyzed by calculating the medians and the spread.

Note that in the calculation of Eq. (B1), the data samples where $F_{30_{POES}} = 0$ while $F_{30_{model}} > 0$, lead to $\epsilon_{F30} = \infty$, and cases where $F_{30_{model}} = 0$ while $F_{30_{POES}} > 0$, give $\epsilon_{F30} = -\infty$. Both these cases, which can be considered respectively over- and underestimations of unknown actual size, have been taken along in the median value calculation, since they do not obstruct it. On the other hand, cases where both $F_{30_{POES}} = 0$ and $F_{30_{model}} = 0$ were not included, since the error cannot be assessed in those cases.

The statistics of ϵ_{F30} for the MLT-independent model are shown as a function of L and Ap in Figure 12. The upper left-hand graph shows the median error. In this graph, the bins for which both the median measured and the median modeled flux was zero, have been excluded. The solid contours indicate differences of 0.5 and −0.5 (i.e. over- and underestimation of the model by a factor of $\sqrt{10}$) and the dotted line indicates an error of 0.

To show the spread to the error, it would be useful to calculate its standard deviation (as a function of L and Ap). However, this is not possible, due to the occurrence of zeros in both the measured and modeled data, which give values of ∞ and $-\infty$ respectively (as explained above). The occurrence of these data points in any distribution would cause the standard deviation of the distribution to be infinite. Because of this, the spread of the error distribution was calculated as the difference between the 69- and 31-percentiles, i.e. the range covered by the central 38% of values. For a Gaussian distribution, this value is equal to the standard deviation. However, for an arbitrary shaped distribution, this value is not affected by outliers, even if they are $\pm\infty$, as long as the 69- and 31-percentiles are not within the outliers.

The spread (estimated standard deviation) of the error distributions according to this formulation is shown in the upper right-hand graph of Figure 12. Here, the contour indicates a value of 1. The bins for which both the median measured and the median modeled flux was zero are also excluded here. Furthermore, in this figure the black color indicates that the values of the 69- or 31-percentiles were ∞ or $-\infty$, so that the spread could not be calculated this way. This happened particularly in the areas where the fluxes are low so that a significant fraction of the measured samples are zero. In these cases, since the distribution is so irregularly shaped, the median is not considered representative either, and also those bins were excluded from the graph of the medians.

These graphs show that, apart from the unknown errors at the edges, in most of the range where the median ϵ_{F30} can be calculated, it is varying around zero within ± 0.2 (i.e. a median modeling error of F_{30} of less than a factor of 1.6), indicating a good agreement between the model and the median of the measurements. Near the edge at low L values and low Ap values, where the fluxes are low, the model may underestimate the measured flux. This is due to the fact that in these areas, the measured flux was low enough to be considered inaccurate, and the model was intentionally aimed at avoiding overestimations.

The spread is mostly smaller than 1.0 when fluxes are high, indicating that 38% of the modeling errors vary within less than a factor 10 from the median error, i.e. at most a factor $\sqrt{10}$ above or below the median. The spread is somewhat larger, up to 1.4, for moderate to low fluxes ($Ap < 10$ or $L > 7$), due to the increased portion of low-flux data in the bins, which suffer from inaccuracies as explained before.

Around $Ap = 80$ the error is larger than elsewhere and the spread is irregular, which is probably affected by substorms, as was noted in Figure 1.

In order to show the performance of the model in predicting fluxes at higher energy levels, the integrated >300 keV flux F_{300} was additionally analyzed. In both the measured and modeled datasets, F_{300} was calculated from F_{30} and k using the following formula, which follows directly from the equations in Section 2.2:

$$F_{300} = \begin{cases} F_{30}\left(\dfrac{1000^{k+1} - 300^{k+1}}{1000^{k+1} - 30^{k+1}}\right) & (k \neq -1) \\ F_{30}\left(\dfrac{ln(1000) - ln(300)}{ln(1000) - ln(30)}\right) & (k = -1). \end{cases} \tag{B2}$$

Furthermore, just as for F_{30} in Eq. (6), the clause is added that the modeled $F_{300} = 0$ whenever its value resulting from Eq. (B2) is below 10 electrons/(cm^2 s sr). The parameter F_{300} is affected by both modeling parameters F_{30} and k, so that its prediction error can say something about the performance of the model in both parameters.

The modeling error ϵ_{F300} of F_{300} was calculated similarly as Eq. (B1), and the result was again evaluated by calculating the median and the spread for every bin of Ap and L. The result is shown in the lower two graphs of Figure 12.

There are relatively many cases where $\epsilon_{F300} = -\infty$. These are cases of very low flux, where the modeled $F_{300} = 0$ while the measured F_{300} is small but above zero. Because of this, in many bins the 31-percentile and/or the median is $-\infty$ (excluded in the bottom left-hand graph; black in the bottom right-hand graph). In these cases, the prediction performance is unknown. In the rest of the range, it is seen that the median ϵ_{F300} is mostly within ± 0.5 (a factor 3). The spread of these errors is similar to that of ϵ_{F30}.

The performance of the model, particularly for F_{300}, is seen to be somewhat worse for Ap above 60 than below. This is due to the variability found in the measured data for disturbed conditions, which is caused partly by the low numbers of data points measured in those conditions, and partly by the occurrence of substorms, as mentioned above.

The same error analysis has been performed for the MLT-dependent model. Also for this model the modeling errors of F_{30} and F_{300} were binned as a function of Ap and L, and for all MLT together. The medians and spreads of these bins are shown in Figure 13. Also here, bins where the spread is ∞ are excluded from the graph of the medians.

Comparing this with Figure 12, the model would seem to perform much worse than the MLT-independent model. Note however that the data sets are not comparable: the data for Figure 13 were not zonally averaged and therefore less smooth, as explained before. This variability of the data explains part of the variation in the difference between the model and the data. Furthermore, because of this reason, the MLT-dependent model was less aimed at following the behavior of the data exactly, but only the main features, as explained in Section 3.2.

In spite of this, it can be seen than where the fluxes are large, both median modeling errors are smaller than a factor $\sqrt{10}$, and the spreads are mostly around 1, indicating that roughly 38% of the modeling errors are within a factor of 10. For $L > 7.5$, the model mostly overestimates F_{30}, and its spread is larger, due to the fact that the low fluxes measured there were considered unreliable in the MLT-dependent dataset and the dependence on L was not modeled on those data, but on the zonally averaged data (see Section 3.2). The modeling error of F_{300} is somewhat more stable than that of F_{30}.

Also here, the performance of the model is seen to be slightly worse for Ap above 60 than below, for the same reasons as in Figure 12.

The errors analyzed in this Appendix can also be seen as representing the modeling errors in ionization rates, as follows. Since higher-energy electrons ionize generally at lower altitudes, energy levels roughly translate to altitudes. Electrons of 30 keV cause most ionization at 90–100 km and those at 300 keV at 70–80 km, so that Figures 12 and 13 also represent the errors in ionization rates of both models at those altitudes.

Appendix C: Comparison with previous model

The Ap-dependent flux model previously published by *van de Kamp et al.* [2016] is part of the recommendation for the CMIP6 forcing datasets [*Matthes et al.*, 2017]. It is therefore being used in atmospheric models, and probably will still be used for some time. For this reason it is useful to demonstrate the difference between that model and the MLT-independent model developed in the current study. This allows an assessment of the expected impact if the previous model is replaced by the new. As stated in Section 1.2, the new model was developed to provide a more realistic modeling of low fluxes during quiet times, which may have been overestimated in the previous model due to the noise in the measurements which the model was based on.

Figure 14 shows F_{30} and k as given by the previous model, calculated in exactly the same procedure as the new model in Figure 4: for the time period of the dataset used in this paper, binned for the same Ap and k values as Figure 4, and the medians calculated for every bin. Comparing this figure to Figure 4, it can be seen that in moderate to disturbed times ($Ap > 10$) F_{30} is mostly similar, and the main difference is that the new model gives lower fluxes during quiet times, as expected. In the gradient k also some differences are seen, the significance of which will be discussed below.

In order to compare the flux levels as predicted by both models over the full energy spectrum, we have calculated the flux spectral density $S(E)$, which in the radiation belt community is more commonly referred to as the differential electron flux. $S(E)$ is defined by equation (1), with C given by (derived from Eq. (2)):

$$C = \begin{cases} \dfrac{F_{30}(k+1)}{(E_U^{k+1} - 30^{k+1})} & (k \neq -1) \\ \dfrac{F_{30}}{ln(E_U) - ln(30)} & (k = -1) \end{cases} . \tag{C1}$$

with $E_U = 1000$ (keV). This was calculated from F_{30} and k as given by both models, for Ap from 1 to 100 and L from 2 to 10, and S_{pp} given by Eqs. (4)-(5). In order to be independent of the time parameter, we used $ln\, Ap$ instead of $ln\, max_{t-1,t}\, Ap$ in Eq. (5). Next, the difference in S between both models was calculated as

$$\text{Difference} = log_{10}S(E)_{2016} - log_{10}S(E)_{2018} \tag{C2}$$

where '2016' refers to the previous model and '2018' to the model presented in the current paper. Figure 15 shows the difference thus found, as a function of Ap and L, for three values of the energy E. Similarly as in Figures 12-13, the dotted contours indicate the value of 0, and the solid contours values of ± 0.5 (a factor $\sqrt{10}$ difference in S).

This Figure shows that during moderate to disturbed times ($Ap > 10$), the difference between the models is smallest. In the middle of the radiation belt it is even less than 0.5. Outside of this, where fluxes are lower, the differences are a bit larger and show some variation with E, which is due to the differences seen in the spectral gradient noted when comparing the right-hand graphs of Figures 4 and 14. It is however useful to note that as long as $Ap > 10$, the difference between the models is smaller than the spread in the error of the new model, as shown in the right-hand graphs of Figure 12. This spread is caused by the spread in the data, and represents the uncertainty of any model which predicts the flux based on Ap and L. Therefore, Figure 15 shows that for $Ap > 10$, both models agree within this uncertainty.

For quiet times ($Ap < 10$), the new model gives a consistently lower flux than the old model for all energy levels. This was the intended upgrade of the model, i.e. a more careful modeling of low fluxes, and demonstrates that the old model may overestimate low fluxes during quiet times by a factor of 10 or even 100, depending on Ap, L and E. The dependence of the overestimation on E is not very strong.

The dark red color in Figure 15 indicates when F_{30} according to the new model is 0 due to the clause mentioned below Eq. (6), so consequently $C = 0$. The previous model did not have a similar clause.

To have an indication of the difference between the two models in ionization levels at different altitudes, it can be roughly assumed that electrons of 30 keV cause most ionization at 90–100 km, those at 100 keV at 80–90 km, and those at 300 keV at 70–80 km.

Acknowledgments. We thank the Academy of Finland for supporting this research: M. van de Kamp and P. T. Verronen were supported by the project #276926 (SECTIC: Sun-Earth Connection Through Ion Chemistry), A. Seppälä was supported by projects #258165, #265005 and #292806 (CLASP: Climate and Solar Particle Forcing). M. A. Clilverd was supported by the Natural Environmental Research Council grant NE/J008125/1. A. Seppälä , M. A. Clilverd, C. J. Rodger and P. T. Verronen would like to thank the International Space Science Institute (ISSI), Bern, Switzerland for supporting the "Quantifying Hemispheric Differences in Particle Forcing Effects on Stratospheric Ozone team (Leader: D. R. Marsh). The NOAA/POES data used in this study are available from the National Oceanic and Atmospheric Administration (https://www.class.ncdc.noaa.gov). The Ap index is available from ftp://ftp.ngdc.noaa.gov/STP/GEOMAGNETIC_DATA/INDICES/KP_AP/ . The NRLMSISE-00 model can be obtained from https://ccmc.gsfc.nasa.gov/modelweb/models/nrlmsise00.php .

References

Arsenovic, P., E. Rozanov, A. Stenke, B. Funke, J. M. Wissing, K. Mursula, F. Tummon, and T. Peter (2016), The influence of Middle Range Energy Electrons on atmospheric chemistry and regional climate, *J. Atmos. Sol.-Terr. Phys.*, 149, 180-190, doi:10.1016/j.jastp.2016.04.008.

Asikainen, T., and K. Mursula (2013), Correcting the NOAA/MEPED energetic electron fluxes for detector efficiency and proton contamination, *J. Geophys. Res. Space Physics*, 118, 6500 6510, doi:10.1002/jgra.50584.

Brasseur, G., and S. Solomon (2005), *Aeronomy of the Middle Atmosphere: Chemistry and Physics of the Stratosphere and Mesosphere*, 3rd ed. Springer, Dordrecht.

Carson, B. R., C. J. Rodger, and M. A. Clilverd (2013), POES satellite observations of EMIC-wave driven relativistic electron precipitation during 1998-2010, *J. Geophys. Res. Space Physics*, 118, 232–243, doi:10.1029/2012JA017998.

Clilverd, M. A., C. J. Rodger, R. J. Gamble, T. Ulich, T. Raita, A. Seppälä, J. C. Green, N. R. Thomson, J.-A. Sauvaud, and M. Parrot (2010), Ground-based estimates of outer radiation belt energetic electron precipitation fluxes into the atmosphere, *J. Geophys. Res.*, 115, A12304, doi:10.1029/2010JA015638.

Codrescu, M. V., T. J. Fuller-Rowell, R. G. Roble and D. S. Evans (1997), Medium energy particle precipitation influences on the mesosphere and lower thermosphere, *J. Geophys. Res.*, 102 (A9), 19,977–19,987.

Cole, K. D. (1963), Eccentric Dipole Coordinates, *Aust. J. Phys.*, 16, 423-429.

Cresswell-Moorcock, K., C. J. Rodger, A. Kero, A. B. Collier, M. A. Clilverd, I. Häggström, and T. Pitkänen (2013), A reexamination of latitudinal limits of substorm-produced energetic electron precipitation, *J. Geophys. Res.*, *118*(1), 6694–6705, doi:10.1002/jgra.50598.

Evans, D. S. and M. S. Greer (2004), Polar Orbiting Environmental Satellite Space Environment Monitor - 2: Instrument Descriptions and Archive Data Documentation, *NOAA Tech. Mem. 1.4*, Space Environment Center, Boulder, Co.

Fang, X., C. E. Randall, D. Lummerzheim, W. Wang, G. Lu, S. C. Solomon, and R. A. Frahm (2010), Parameterization of monoenergetic electron impact ionization, *Geophys. Res. Lett.*, 37, L22106, doi:10.1029/2010GL045406.

Fraser-Smith, A. C. (1987), Centered and Eccentric Geomagnetic Dipoles and Their Poles, 1600-1985, *Rev. Geophys.*, 25, 1-16.

Hargreaves, J. K., M. J. Birch, and D. S. Evans (2010), On the fine structure of medium energy electron fluxes in the auroral zone and related effects in the ionospheric D region, *Ann. Geophys.*, 28, 11071120, doi:10.5194/angeo-28-1107-2010.

Hartz, T. R. and N. M. Brice (1967), The general pattern of auroral particle precipitation, *Planet. Space Sci.*, 15(2), 301-329.

Horne, R. B., M. M. Lam, and J. C. Green (2009), Energetic electron precipitation from the outer radiation belt during geomagnetic storms, *Geophys. Res. Lett.*, 36, L19104, doi:10.1029/2009GL040236.

Jackman, C. H., Marsh, D. R., Vitt, F. M., Garcia, R. R., Fleming, E. L., Labow, G. J., Randall, C. E., López-Puertas, M., Funke, B., von Clarmann, T., and Stiller, G. P. (2008), Short- and medium-term atmospheric constituent effects of very large solar proton events, *Atmos. Chem. Phys.*, 8(3), 765–785, doi:10.5194/acp-8-765-2008.

Jackman, C. H., D. R. Marsh, F. M. Vitt, R. R. Garcia, C. E. Randall, E. L. Fleming, and S. M. Frith (2009), Long-term middle atmospheric influence of very large solar proton events, *J. Geophys. Res.*, 114, D11304, doi:10.1029/2008JD011415.

Lam, M. M., R. B. Horne, N. P. Meredith, S. A. Glauert, T. Moffat-Griffin, and J. C. Green (2010), Origin of energetic electron precipitation ¿30 keV into the atmosphere, *J. Geophys. Res.*, 115, A00F08, doi:10.1029/2009JA014619.

Matthes, K., B. Funke, M. E. Anderson, L. Barnard, J. Beer, P. Charbonneau, M. A. Clilverd, T. Dudok de Wit, M. Haberreiter, A. Hendry, C. H. Jackman, M. Kretschmar, T. Kruschke, M. Kunze, U. Langematz, D. R. Marsh, A. Maycock, S. Misios, C. J. Rodger, A. A. Scaife, A. Seppälä, M. Shangguan, M. Sinnhuber, K. Tourpali, I. Usoskin, M. van de Kamp, P. T. Verronen, and S. Versick (2017), Solar Forcing for CMIP6 (v3.2), *Geosci. Model Dev.*, 10, 2247-2302, doi:10.5194/gmd-10-2247-2017.

Meredith, N. P., R. B. Horne, M. M. Lam, M. H. Denton, J. E. Borovsky, and J. C. Green (2011), Energetic electron precipitation during high-speed solar wind stream driven storms, *J. Geophys. Res.*, 116, A05223, doi:10.1029/2010JA016293.

Neal, J. J., C. J. Rodger, and J. C. Green (2013), Empirical determination of solar proton access to the atmosphere: Impact on polar flight paths, *Space Weather*, 11, 420–433, doi:10.1002/swe20066.

Neal, J. J., C. J. Rodger, M. A. Clilverd, N. R. Thomson, T. Raita, and Th. Ulich (2015), Long-term determination of energetic electron precipitation into the atmosphere from AARDDVARK subionospheric VLF observations, *J. Geophys. Res.*, 120, 21942211, doi: 10.1002/2014JA020689.

Nesse Tyssøy, H. and J. Stadsnes (2015), Cutoff latitude variation during solar proton events: Causes and consequences, *J. Geophys. Res. Space Physics*, 120, 553-563, doi: 10.1002/2014JA020508.

Nesse Tyssøy, H., M. I. Sandanger, L.-K. G. Ødegaard, J. Stadsnes, A. Aasnes, and A. E. Zawedde (2016), Energetic electron precipitation into the middle atmosphereConstructing the loss cone fluxes from MEPED POES, *J. Geophys. Res. Space Physics*, 121, 56935707, doi:10.1002/2016JA022752.

O'Brien, T. P. and M. B. Moldwin (2003), Empirical plasmapause models from magnetic indices, *Geophys. Res. Lett.*, 30(4), 1152, doi:10.1029/2002GL016007.

Ødegaard, L.-K. G., H. N. Tyssøy, F. Sraas, J. Stadsnes, and M. I. Sandanger (2017), Energetic electron precipitation in weak to moderate corotating interaction region-driven storms, *J. Geophys. Res. Space Physics*, 122, 2900-2921, doi:10.1002/2016JA023096.

Parrot, M. and C. A. Gaye (1994), A statistical survey of ELF waves in a geostationary orbit, *Geophys. Res. Lett.*, 21(23), 2463-2466.

Peck, E. D., C. E. Randall, J. C. Green, J. V. Rodriguez, and C. J. Rodger (2015), POES MEPED differential flux retrievals and electron channel contamination correction, *J. Geophys. Res. Space Physics*, 120, 45964612, doi:10.1002/2014JA020817.

Picone, J. M., A. E. Hedin, D. P. Drob, and A. C. Aikin (2002), NRLMSISE-00 empirical model of the atmosphere: Statistical comparisons and scientific issues, *J. Geophys. Res.*, 107(A12), 1468, doi:10.1029/2002JA009430.

Randall, C. E., D. W. Rusch, R. M. Bevilacqua, K. W. Hoppel, and J. D. Lumpe (1998), Polar Ozone and Aerosol Measurement (POAM) II stratospheric NO2, 1993 1996, *J. Geophys. Res.*, 103(28), 361 28, 372.

Randall, C. E., V. L. Harvey, L. A. Holt, D. R. Marsh, D. E. Kinnison, B. Funke, and P. F. Bernath (2015), Simulation of energetic particle precipitation effects during the 2003–2004 Arctic winter, *J. Geophys. Res.*, 120(6), 5035–5048, doi:10.1002/2015JA021196.

Rodger, C. J., M. A. Clilverd, J. C. Green, and M. M. Lam (2010a), Use of POES SEM-2 observations to examine radiation belt dynamics and energetic electron precipitation into the atmosphere, *J. Geophys. Res.*, 115, A04202, doi:10.1029/2008JA014023.

Rodger, C. J., B. R. Carson, S. A. Cummer, R. J. Gamble, M. A. Clilverd, J-A. Sauvaud, M. Parrot, J. C. Green, and J.-J. Berthelier (2010b), Contrasting the efficiency of radiation belt losses caused by ducted and non-ducted whistler mode waves from ground-based transmitters, *J. Geophys. Res.*, 115, A12208, doi:10.1029/2010JA015880.

Rodger, C. J., M. A. Clilverd, A. Seppälä, N. R. Thomson, R. J. Gamble, M. Parrot, J. A. Sauvaud and Th. Ulich (2010c), Radiation belt electron precipitation due to geomagnetic storms: significance to middle atmosphere ozone chemistry, *J. Geophys. Res.*, 115, A11320, doi:10.1029/2010JA015599.

Rodger, C. J., A. J. Kavanagh, M. A. Clilverd, and S. R. Marple (2013), Comparison between POES energetic electron precipitation observations and riometer absorptions: Implications for determining true precipitation fluxes, *J. Geophys. Res. Space Physics*, 118, doi:10.1002/2013JA019439.

Rozanov, E., M. Calisto, T. Egorova, T. Peter, and W. Schmutz (2012), Influence of the Precipitation Energetic particles on Atmospheric Chemistry and Climate, *Surv. Geophys.*, 33, 483-501, doi:10.1007/s10712-012-9192-0.

Sauvaud, J. A., T. Moreau, R. Maggiolo, J.P. Treilhou, C. Jacquey, A. Cros, J. Coutelier, J. Rouzaud, E. Penou, and M. Gangloff, (2006), Highenergy electron detection onboard

DEMETER: The IDP spectrometer, description and first results on the inner belt, *Planet. Space. Sci.*, 54(5), 502511.

Seppälä, A., and M. A. Clilverd (2014), Energetic particle forcing of the Northern Hemisphere winter stratosphere: comparison to solar irradiance forcing, *Frontiers in Phys.*, 2(25), doi:10.3389/fphy.2014.00025.

Seppälä, A., K. Matthes, C. E. Randall, and I. A. Mironova (2014), What is the solar influence on climate? Overview of activities during CAWSES-II, *Prog. Earth Planet. Sci.*, 1(1), 24, doi:10.1186/s40645-014-0024-3.

Seppälä, A., C. E. Randall, M. A. Clilverd, E. V. Rozanov, and C. J. Rodger (2009), Geomagnetic activity and polar surface air temperature variability, *J. Geophys. Res.*, 114, A10312, doi:10.1029/2008JA014029.

Seppälä, A., H. Lu, M. A. Clilverd, and C. J. Rodger (2013), Geomagnetic activity signatures in wintertime stratosphere wind, temperature, and wave response, *J. Geophys. Res.*, 118, 2169–2183, doi:10.1002/jgrd.50236.

Summers, D., R. M. Thorne, and F. Xiao (1998), Relativistic theory of wave-particle resonant diffusion with application to electron acceleration in the magnetosphere, *J. Geophys. Res.*, 103(A9), 20487-20500.

Thorne, R. M. (2010), Radiation belt dynamics: The importance of wave-particle interactions, *Geophys. Res. Lett.*, 37, L22107, doi:10.1029/2010GL044990.

Turunen, E., P. T. Verronen, A. Seppälä, C. J. Rodger, M. A. Clilverd, J. Tamminen, C. F. Enell, and Th. Ulich (2009), Impact of different energies of precipitating particles on NO_x generation in the middle and upper atmosphere during geomagnetic storms, *J. Atmos. Sol. Terr. Phys.*, 71, 1176–1189, doi:10.1016/j.jastp.2008.07.005.

van de Kamp, M., A. Seppälä, M. A. Clilverd, C. J. Rodger, P. T. Verronen, and I. C. Whittaker (2016), A model providing long-term data sets of energetic electron precipitation during geomagnetic storms, *J. Geophys. Res. Atmos.*, 121, doi: 10.1002/2015JD024212.

Whittaker, I. C., R. J. Gamble, C. J. Rodger, M. A. Clilverd and J.-A. Sauvaud (2013), Determining the spectra of radiation belt electron losses: Fitting DEMETER electron flux observations for typical and storm times, *J. Geophys. Res. Space Physics*, 118, 7611–7623, doi:10.1002.2013JA019228.

Whittaker, I. C., M. A. Clilverd, and C. J. Rodger (2014a), Characteristics of precipitating energetic electron fluxes relative to the plasmapause during geomagnetic storms, *J. Geophys. Res. Space Physics*, 119, 8784–8800, doi:10.1002/2014JA020446.

Whittaker, I. C., C. J. Rodger, M. A. Clilverd, and J.-A. Sauvaud (2014b), The effects and correction of the geometric factor for the POES/MEPED electron flux instrument using a multisatellite comparison, *J. Geophys. Res. Space Physics*, 119, 63866404, doi: 10.1002/2014JA020021.

Wissing, J. M., J. P. Bornebusch, and M.-B. Kallenrode (2008), Variation of energetic particle precipitation with local magnetic time, *Advances in Space Research*, 41, 1274-1278, doi:10.1016/j.asr.2007.05.063.

Wissing, J. M. and M.-B. Kallenrode, Atmospheric Ionization Model Osnabrück (AIMOS): A 3-D model to determine atmospheric ionization by energetic charged particles from different populations, *J. Geophys. Res.*, 114, A06104, doi:10.1029/2008JA013884.

Wüest, M., R. A. Frahm, J. K. Jennings, and J. R. Sharber (2005), Forecasting electron precipitation based on predicted geomagnetic activity, *Advances in Space Research*, 36, 2445–2450, doi:10.1016/j.asr.2003.12.014.

Yando, K., R. M. Millan, J. C. Green, and D. S. Evans (2011), A Monte Carlo simulation of the NOAA POES Medium Energy Proton and Electron Detector instrument, *J. Geophys. Res.*, 116, A10231, doi:10.1029/2011JA016671.

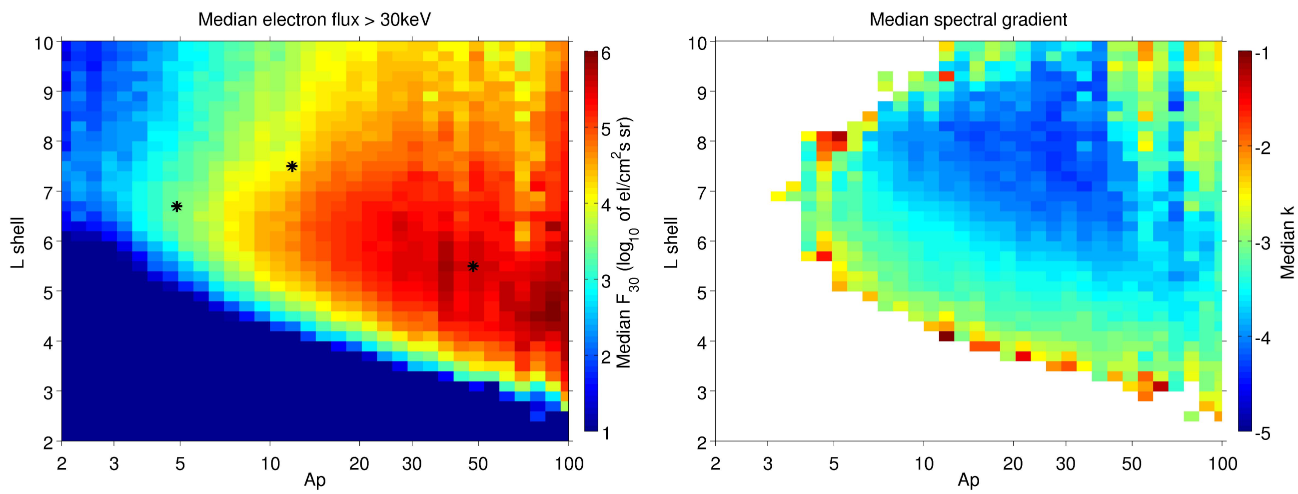

Figure 1. Median flux > 30 keV (left) and median spectral gradient (right), as a function of L and Ap, as resulting from the reanalyzed POES data. The black stars are indicators for the relation with Figures 10 and 11.

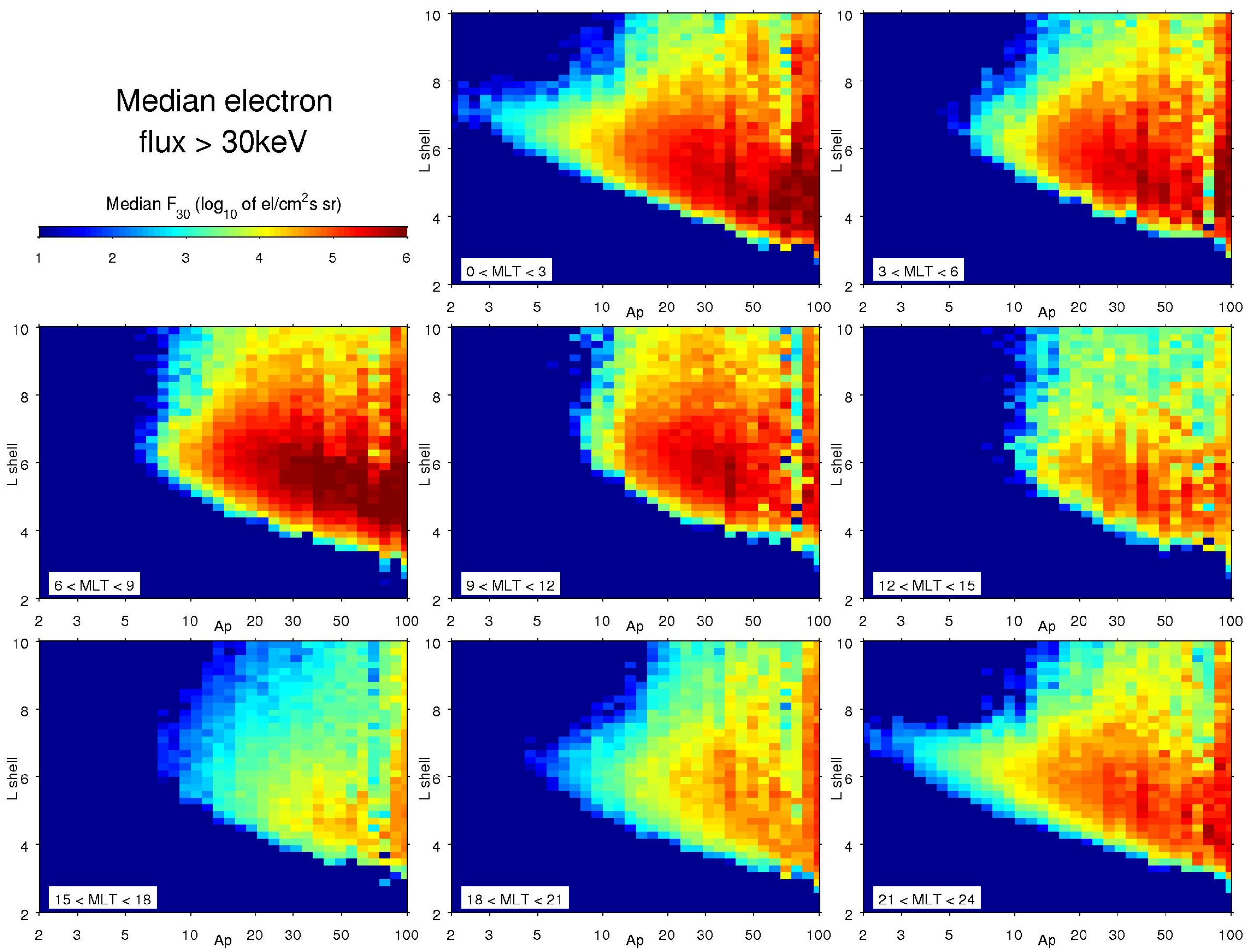

Figure 2. Median flux > 30 keV, as a function of L and Ap for eight MLT zones, as resulting from the reanalyzed POES data.

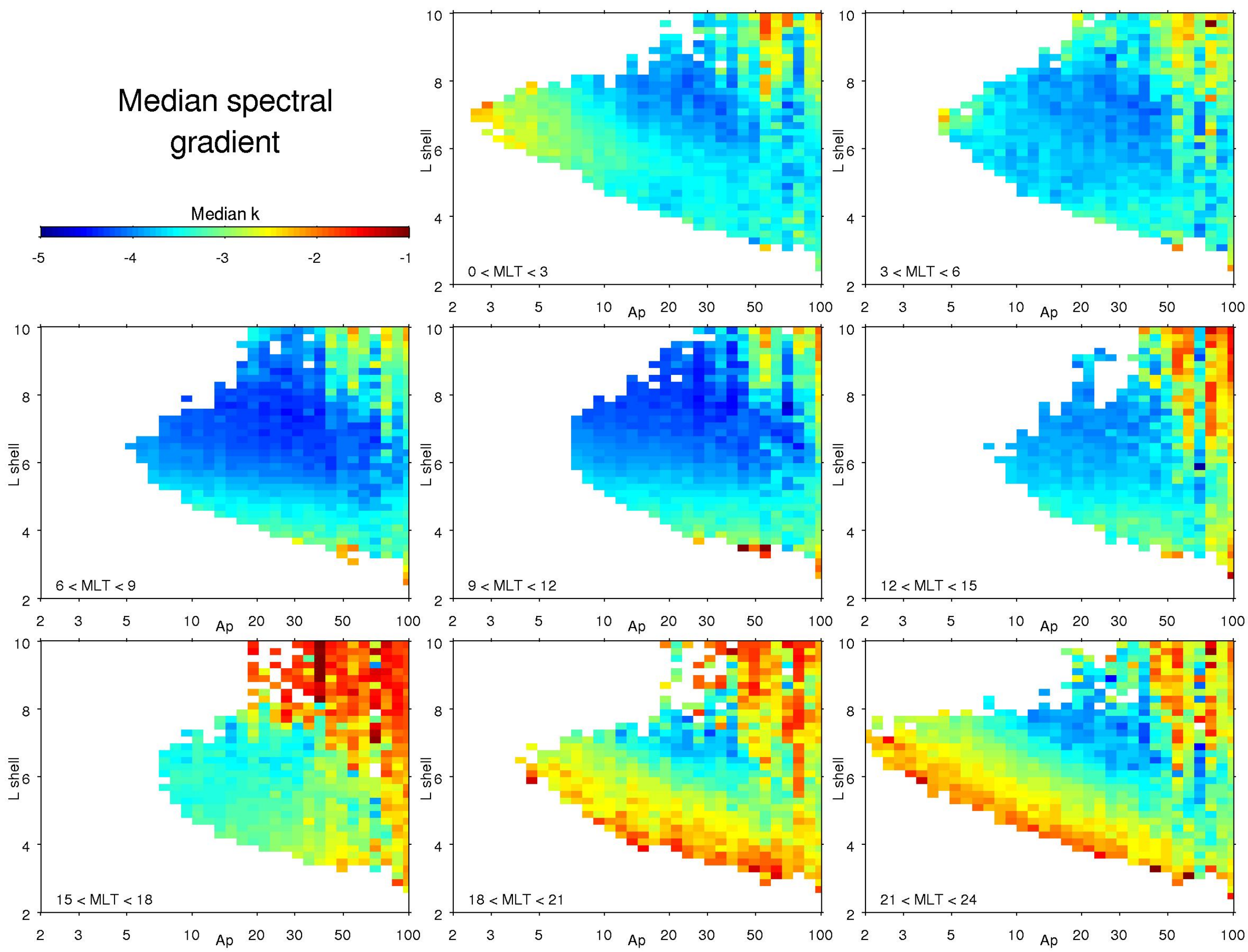

Figure 3. Median spectral gradient, as a function of L and Ap for eight MLT zones, as resulting from the reanalyzed POES data.

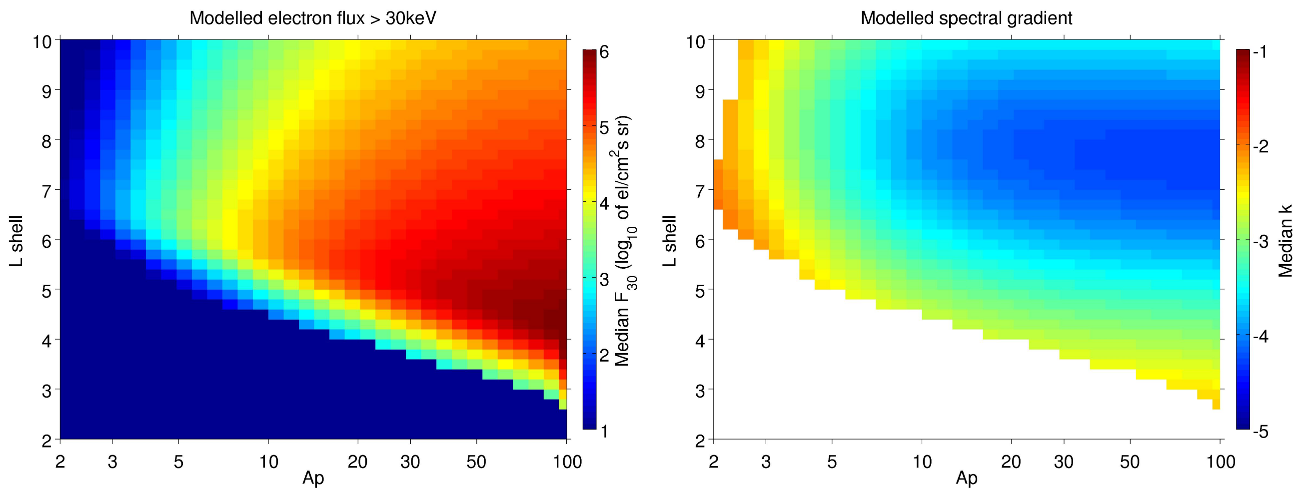

Figure 4. Median modeled flux > 30 keV (left) and median modeled spectral gradient (right), according to Eqs. (6) and (7) (MLT-independent model), as functions of L and Ap.

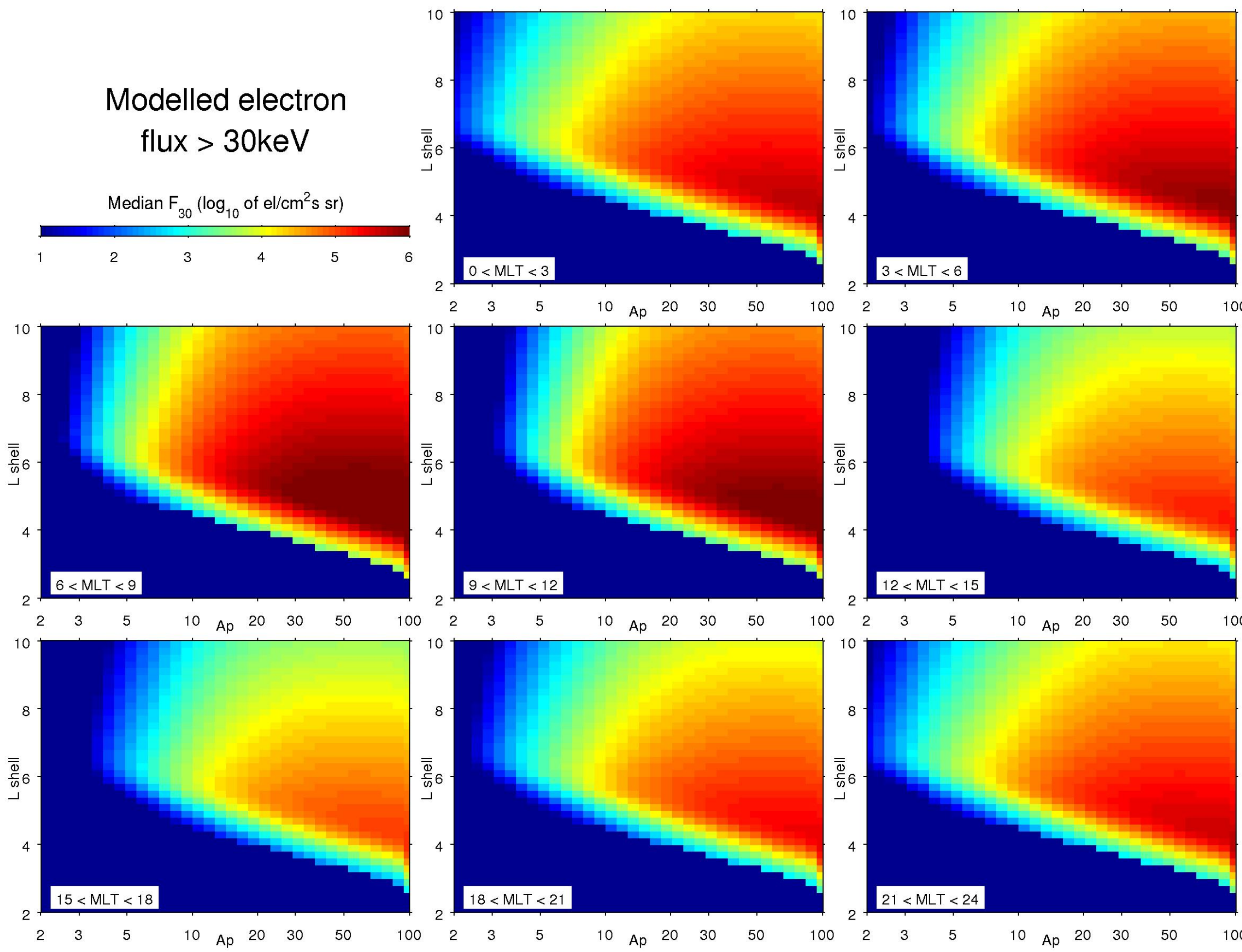

Figure 5. Median modeled flux > 30 keV according to Eq. (8) (MLT-dependent model), as a function of L and Ap for eight MLT zones.

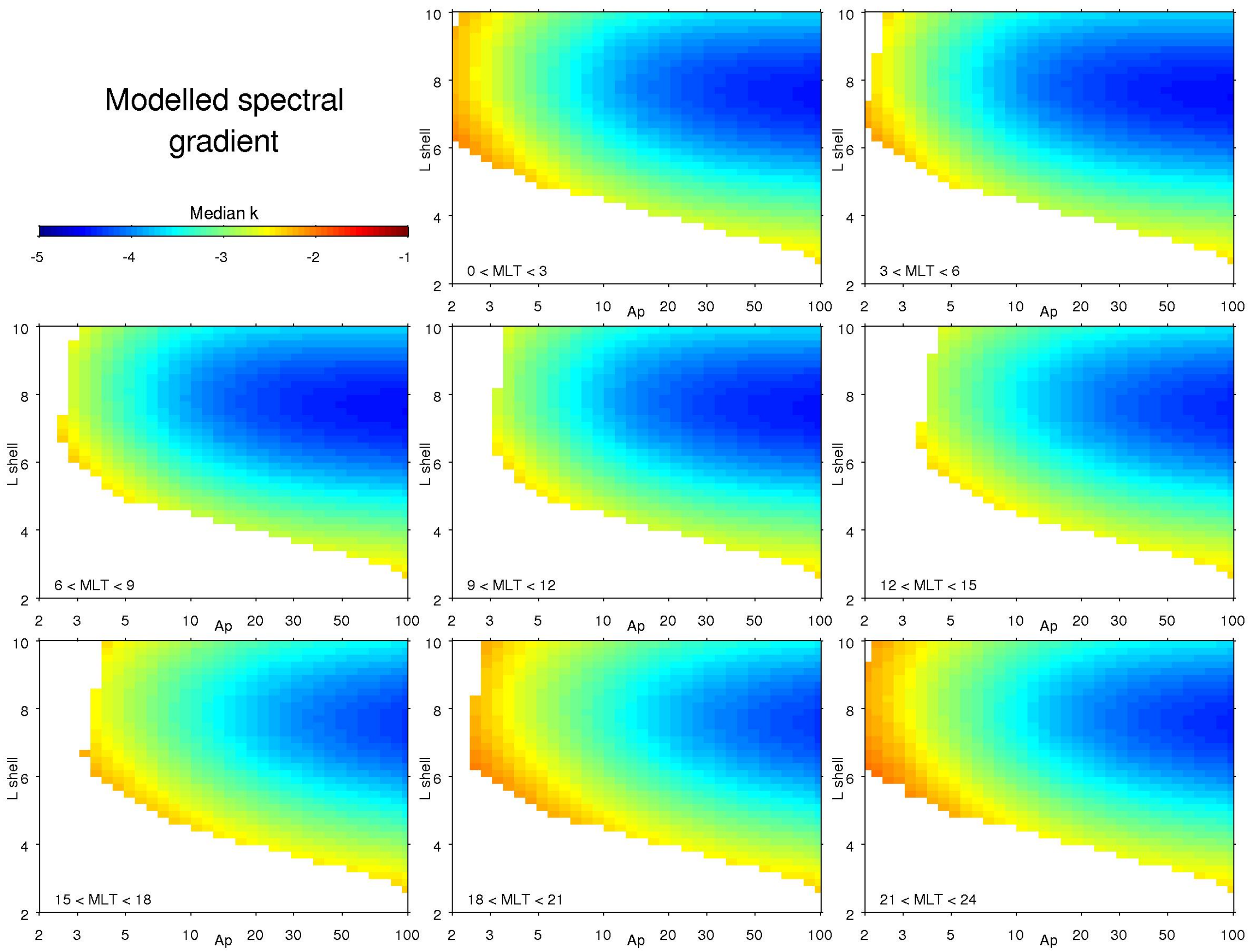

Figure 6. Median modeled spectral gradient according to Eq. (9), as a function of L and Ap for eight MLT zones.

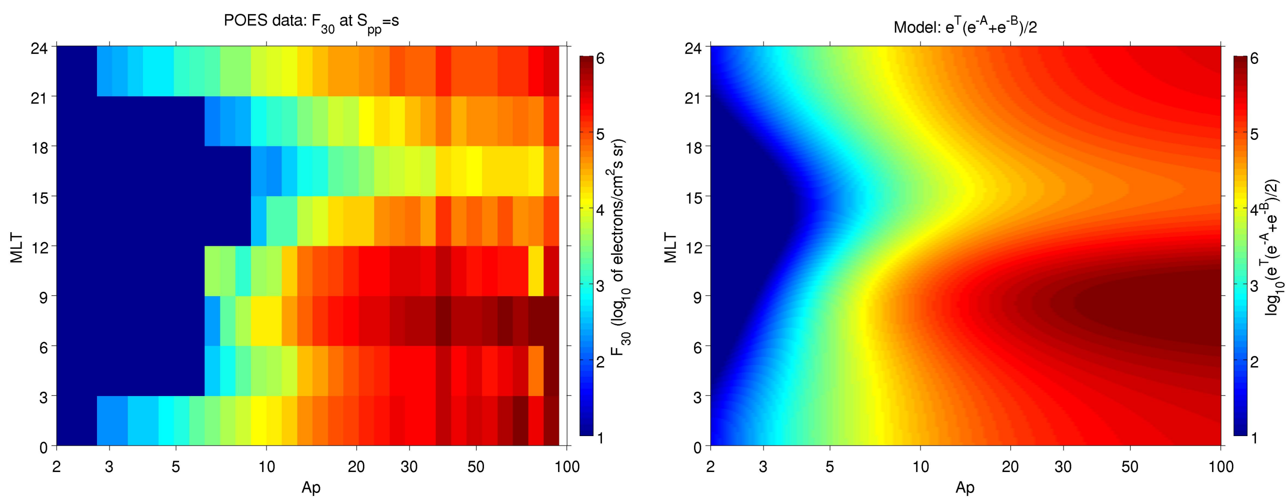

Figure 7. Left: the electron flux > 30 keV F_{30} observed for $s = S_{pp}$, i.e. at the L-value where it peaks, as a function of Ap and MLT. Right: the expression $e^T(e^{-A} + e^{-B})/2$ with A, B and T from Eq. (8), which gives the same peak flux from the MLT-dependent model.

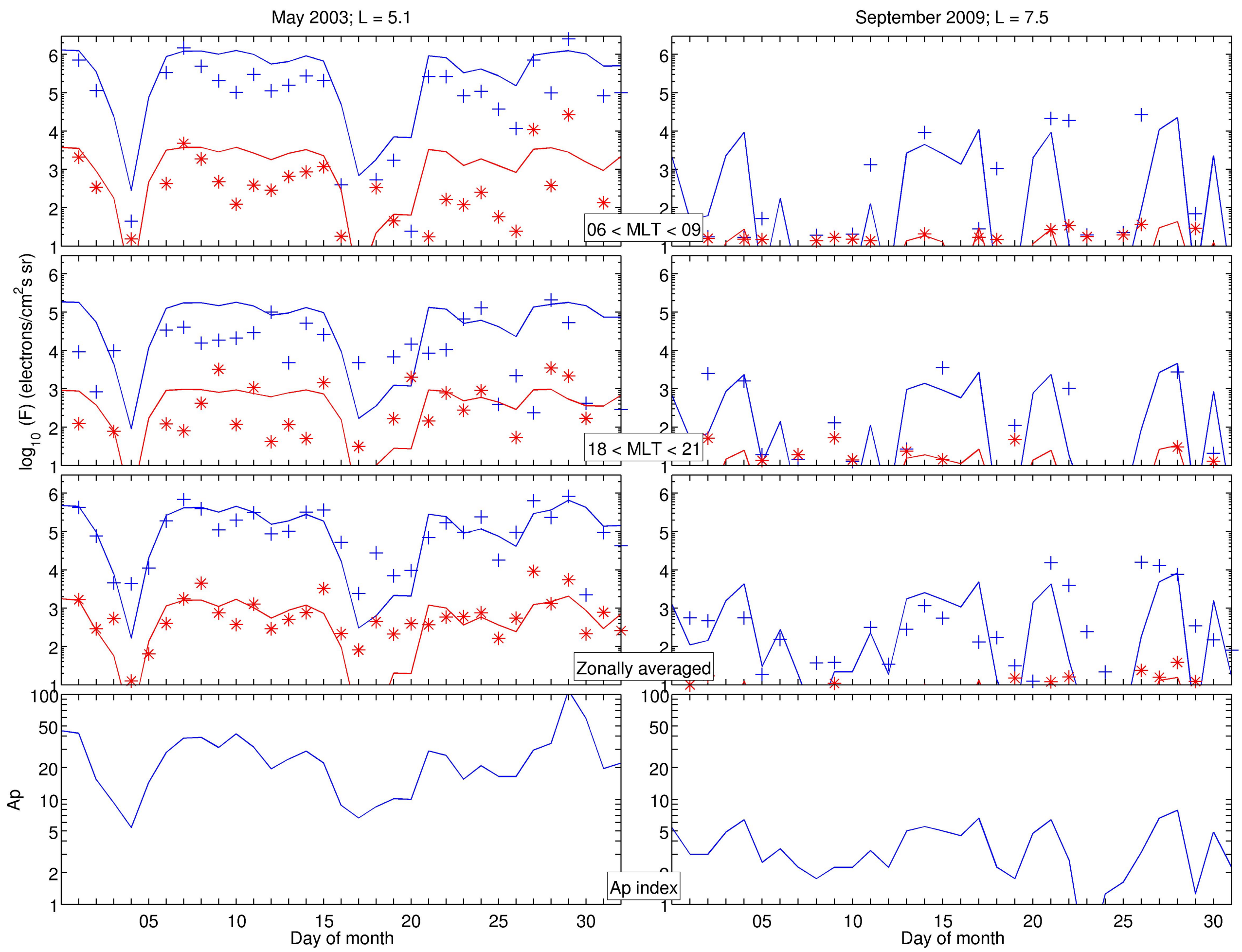

Figure 8. Time series of the POES measured fluxes F_{30} and F_{300} and the fluxes predicted by both models. Left and right column: two different months and two different L-shells (see headers). Upper two rows: data of F_{30} (blue +) and F_{300} (red *) and the MLT-dependent model (blue and red lines) for two different MLTs (see labels between the columns). Third row: zonally averaged data and MLT-independent model. Bottom row: Ap index.

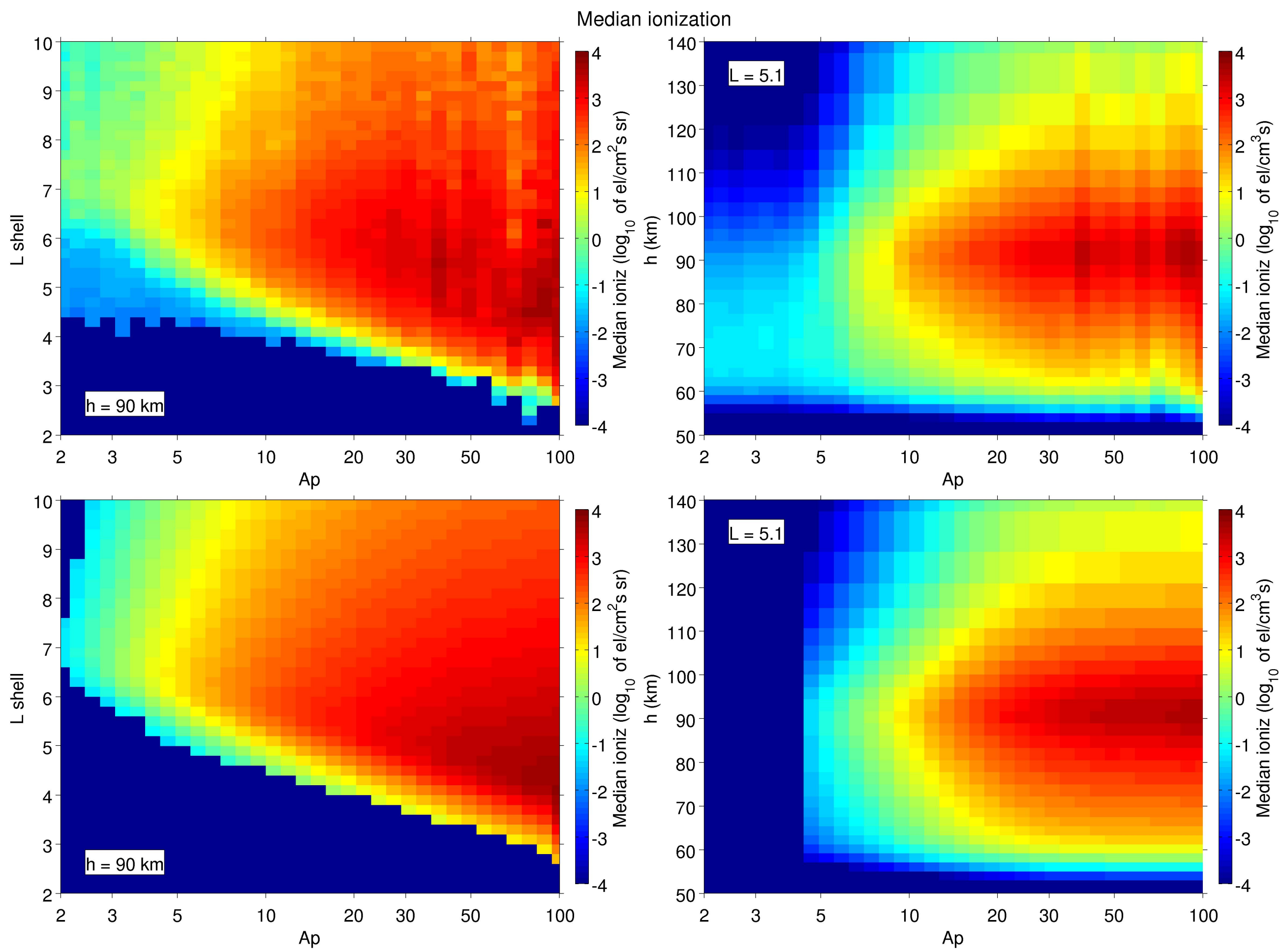

Figure 9. Top row: Median ionization as resulting from the POES observations, as a function of L and Ap at $h = 90$ km (left) and as a function of h and Ap at $L = 5.1$ (right). Bottom row: Median modeled ionization from the MLT-independent model.

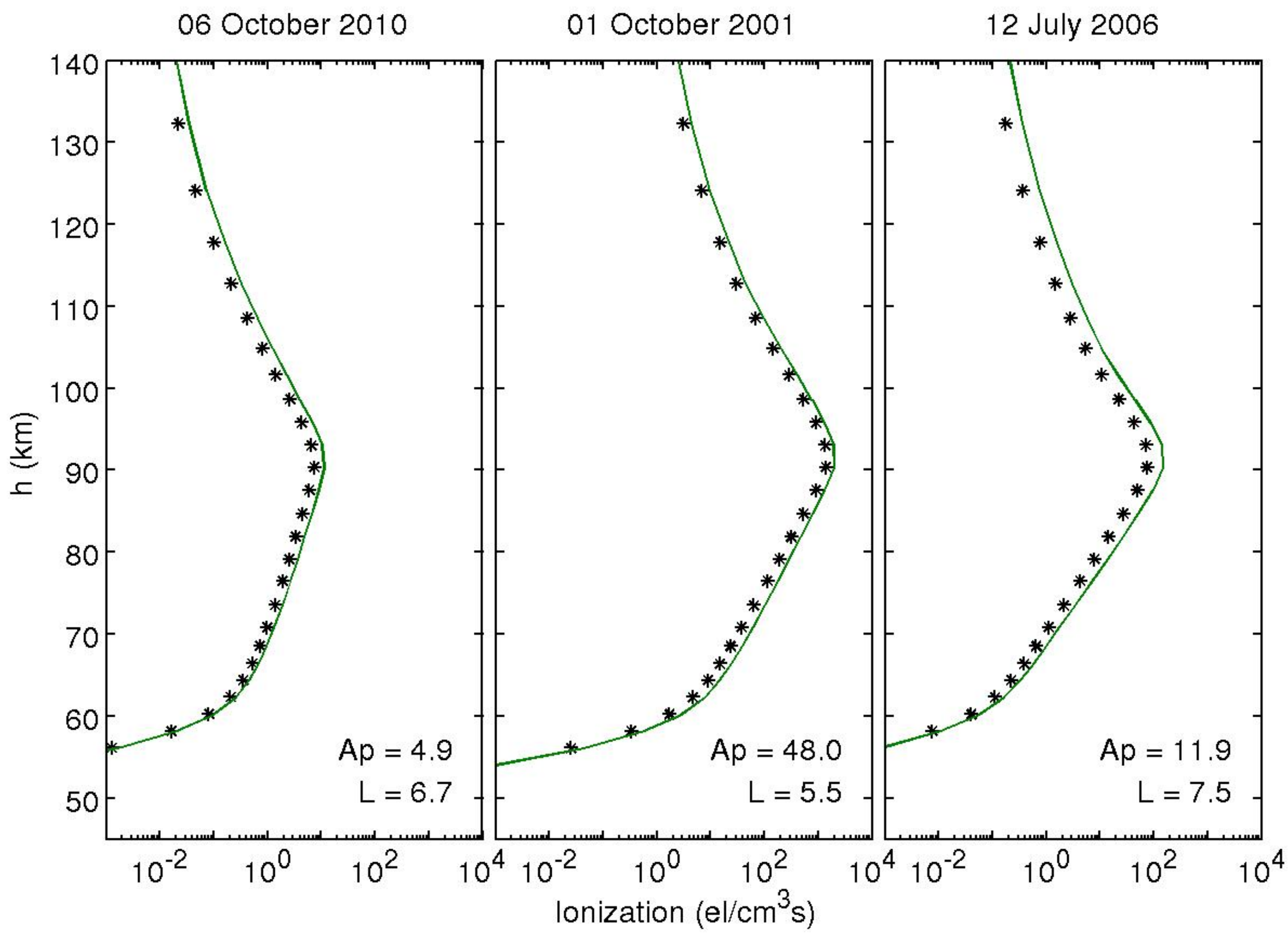

Figure 10. Ionization profiles as functions of h, for three separate days and L-values: according to the MLT-independent model (green line), and the zonally averaged POES observations (stars). The Ap values at the respective days are included in the graphs. These three example cases are marked in Figure 1 as stars.

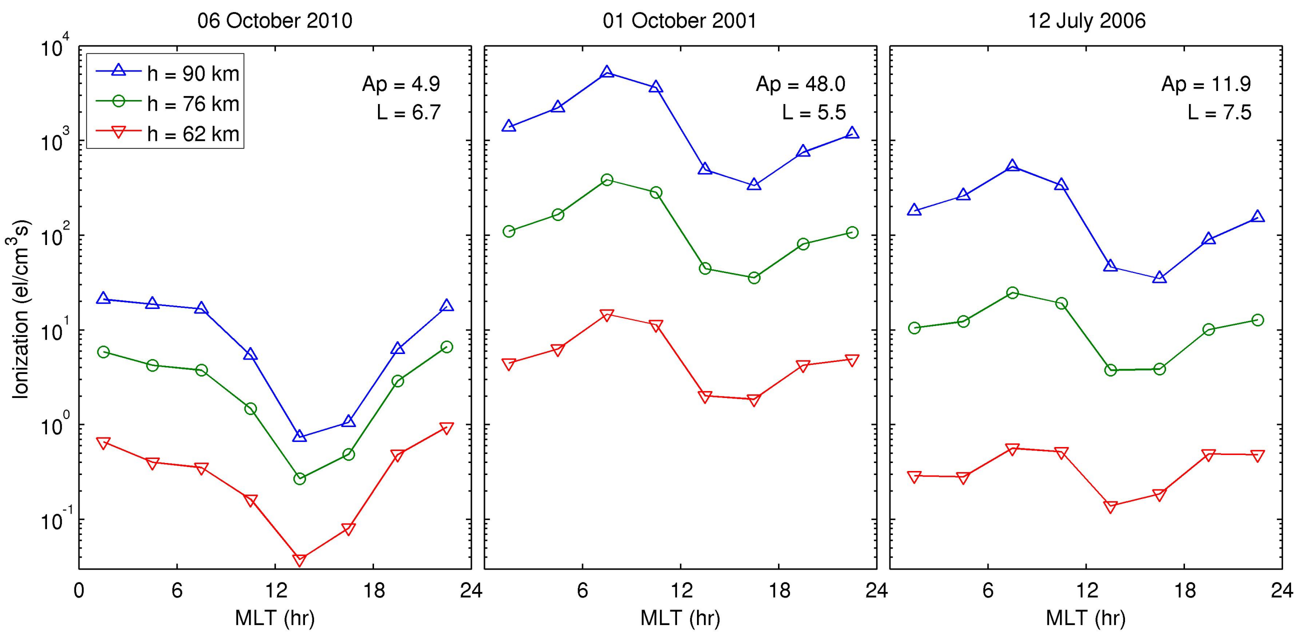

Figure 11. Ionization rates as functions of MLT, at three altitudes, for the same three example cases as Figure 10, according to the MLT-dependent model.

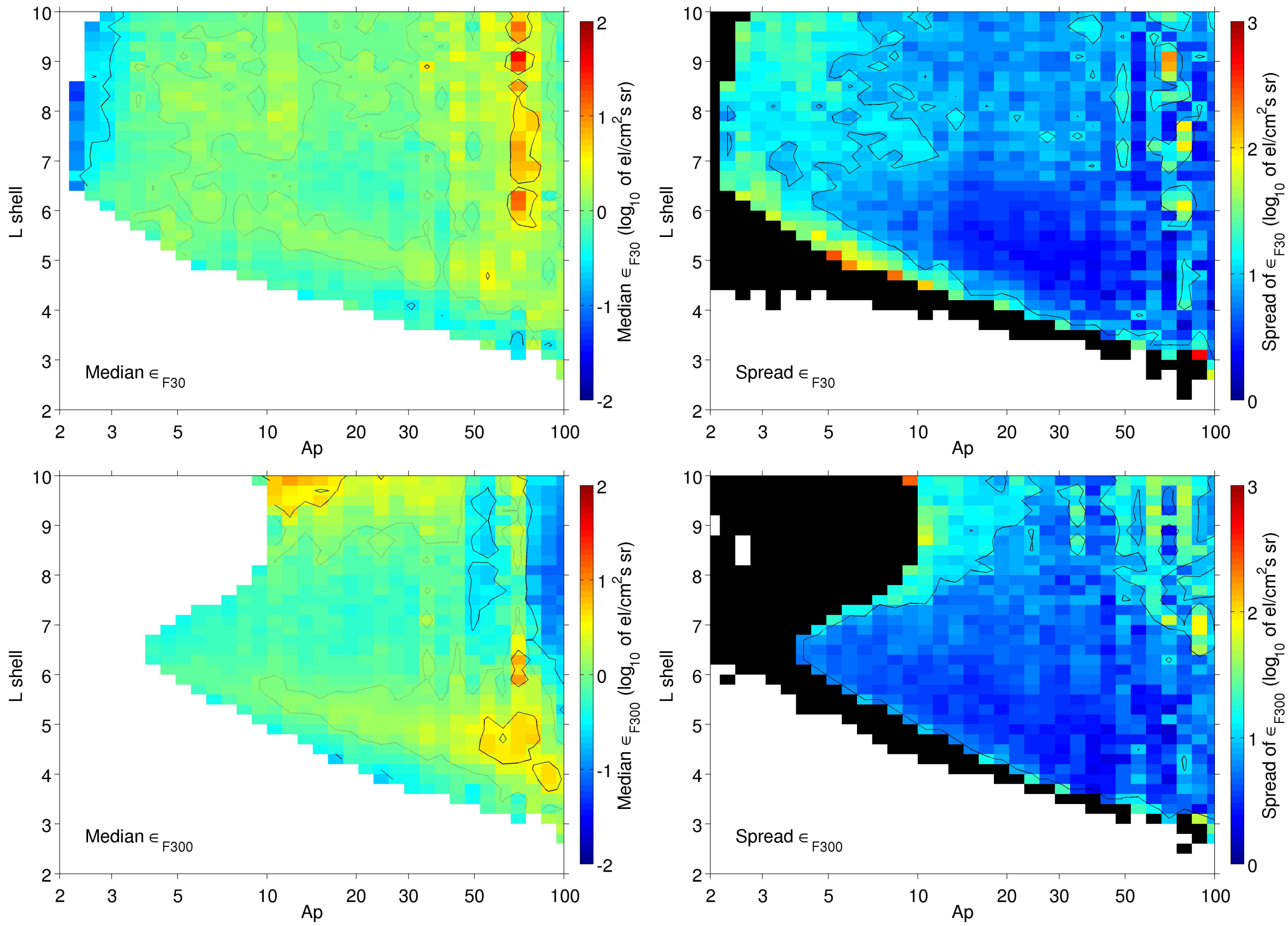

Figure 12. Statistics of the error of the modeled fluxes according to the MLT-independent model. Upper row: the difference ϵ_{F30} between log_{10} of modeled F_{30} and POES flux > 30 keV, as functions of L and Ap. Lower row: the difference ϵ_{F300} in $log_{10}(F_{300})$. Left hand side: medians; the solid contours indicate the values of 0.5 and -0.5; the dotted contours the value of 0. Right-hand side: the spread, represented as the difference between 69- and 31-percentiles (equivalent to a standard deviation in the case of a Gaussian distribution); the contour indicates a value of 1.

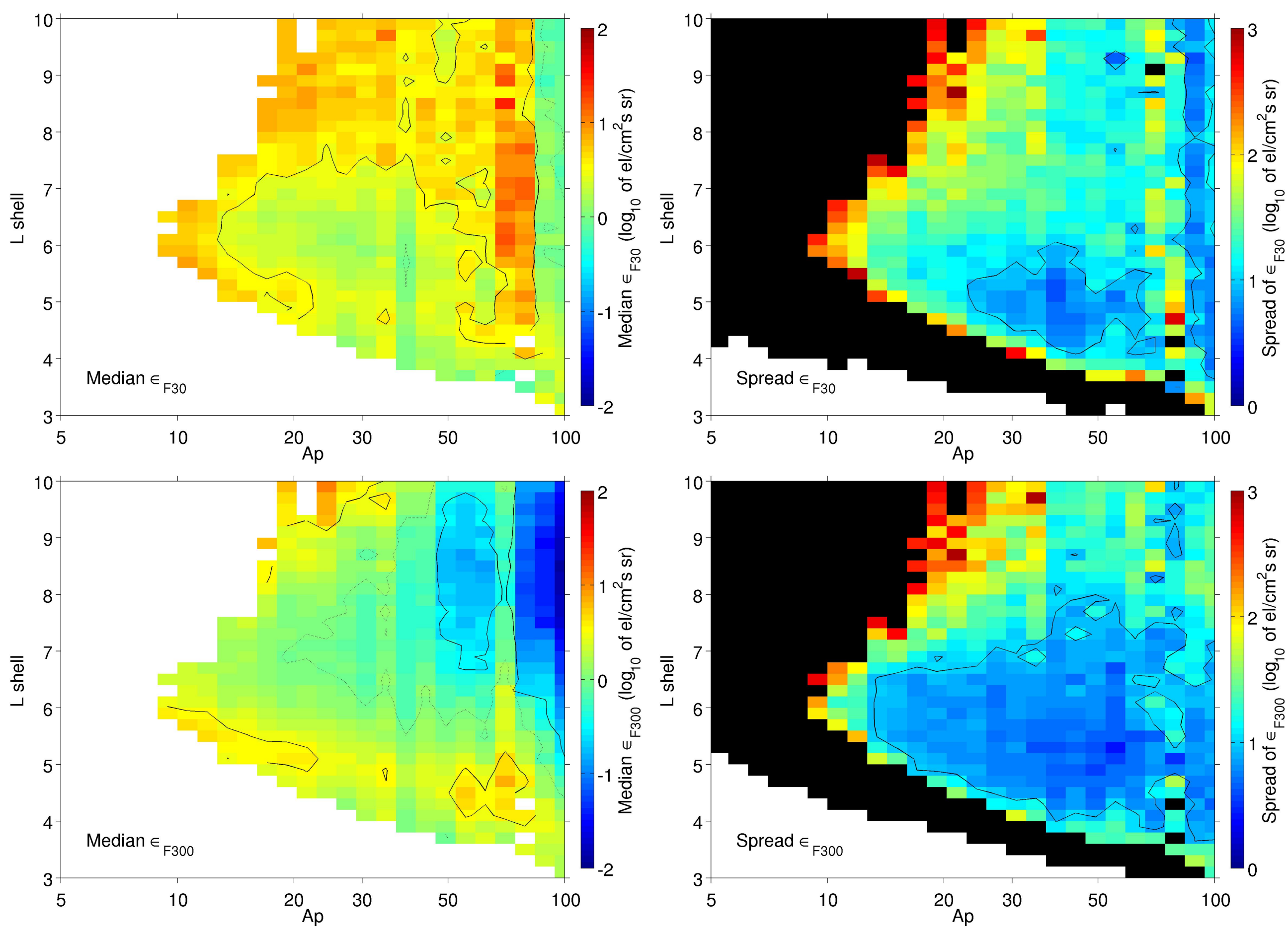

Figure 13. Similar model error statistics as in Figure 12, for the MLT-dependent model. Upper row: the median and the spread of the error of F_{30}. Lower row: the median and the spread of the error of F_{300}.

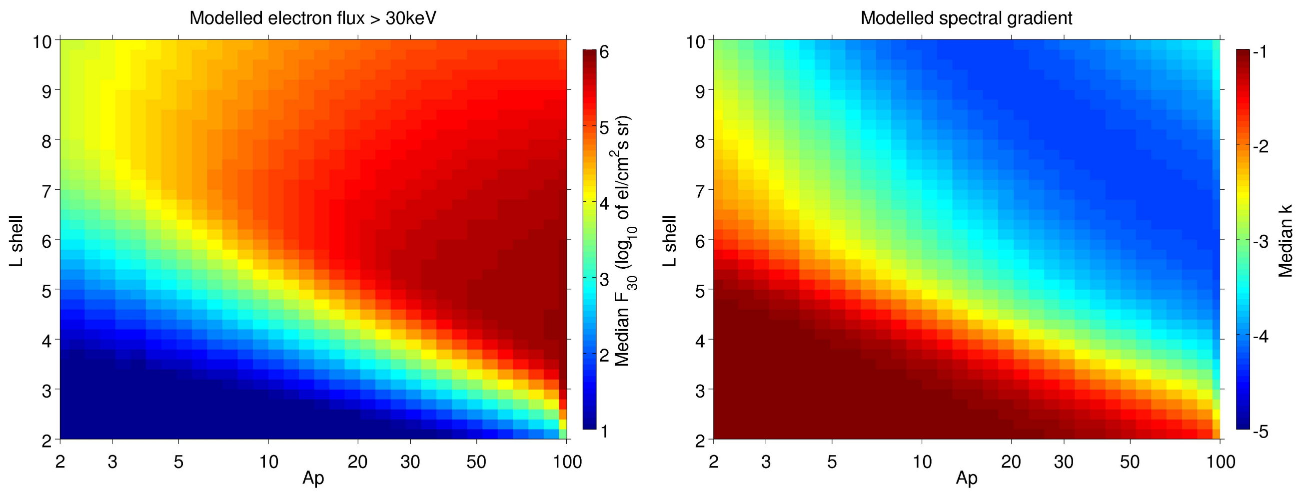

Figure 14. Median modeled flux > 30 keV (left) and median modeled spectral gradient (right), according to the model previously published [*van de Kamp et al.*, 2016] (*Ap*-dependent model), as functions of L and Ap.

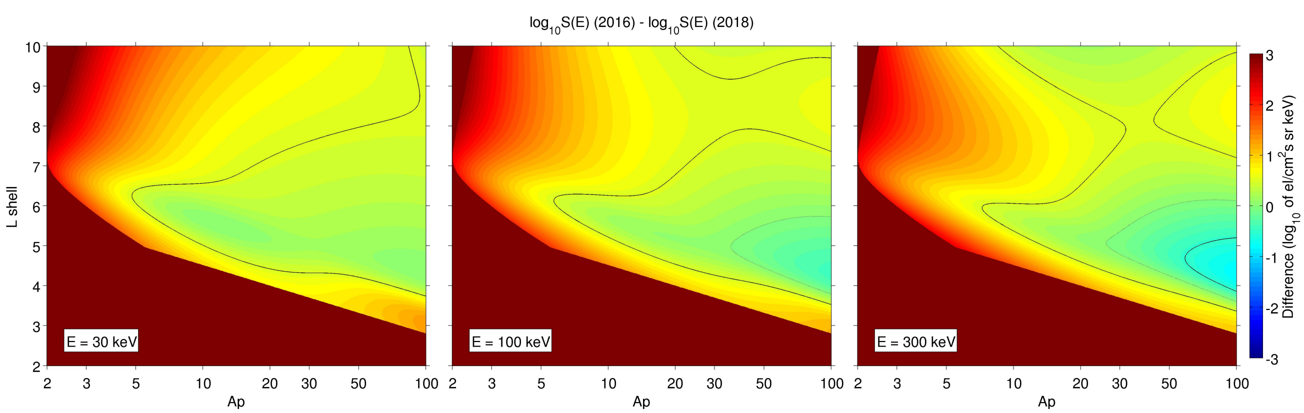

Figure 15. Difference in log_{10} of flux spectral density $S(E)$ between the previous model [*van de Kamp et al.*, 2016] and the MLT-independent model of this paper, for three energy levels.

Figure 1.

Median electron flux > 30keV
L shell
Ap
Median F_{30} ($\log_{10}$ of el/cm^{2}s sr)
Median spectral gradient
L shell
Ap
Median k

Figure 2.

Median electron flux > 30keV
Median F_{30} ($\log_{10}$ of el/cm^{2}s sr)
1 2 3 4 5 6
0 < MLT < 3
3 < MLT < 6
6 < MLT < 9
9 < MLT < 12
12 < MLT < 15
15 < MLT < 18
18 < MLT < 21
21 < MLT < 24
L shell
Ap
2 3 5 10 20 30 50 100
2 4 6 8 10

Figure 3.

Median spectral gradient
Median k
-5
-4
-3
-2
-1
0 < MLT < 3
3 < MLT < 6
6 < MLT < 9
9 < MLT < 12
12 < MLT < 15
15 < MLT < 18
18 < MLT < 21
21 < MLT < 24
L shell
Ap
2
3
5
10
20
30
50
100
4
6
8

Figure 4.

Modelled electron flux > 30keV
L shell
Ap
Median F_{30} ($\log_{10}$ of el/cm^{2}s sr)
Modelled spectral gradient
L shell
Ap
Median k

Figure 5.


Modelled electron flux > 30keV
Median F_{30} ($\log_{10}$ of el/cm^{2}s sr)
1 2 3 4 5 6
L shell
Ap
0 < MLT < 3
3 < MLT < 6
6 < MLT < 9
9 < MLT < 12
12 < MLT < 15
15 < MLT < 18
18 < MLT < 21
21 < MLT < 24

Figure 6.

Modelled spectral gradient
Median k
-5
-4
-3
-2
-1
L shell
Ap
0 < MLT < 3
3 < MLT < 6
6 < MLT < 9
9 < MLT < 12
12 < MLT < 15
15 < MLT < 18
18 < MLT < 21
21 < MLT < 24
2
3
5
10
20
30
50
100
4
6
8

Figure 7.

POES data: F_{30} at S_{pp}=s
Model: $e^{T}(e^{-A}+e^{-B})/2$
MLT
Ap
F_{30} ($\log_{10}$ of electrons/cm^{2}s sr)
$\log_{10}(e^{T}(e^{-A}+e^{-B})/2)$

Figure 8.

May 2003; L = 5.1
September 2009; L = 7.5
06 < MLT < 09
18 < MLT < 21
Zonally averaged
Ap index
log$_{10}$ (F) (electrons/cm^{2}s sr)
Ap
Day of month
Day of month

Figure 9.

Median ionization
L shell
Ap
h = 90 km
Median ioniz (log10 of el/cm2s sr)
h (km)
L = 5.1
Median ionization (log10 of el/cm3s)

Figure 10.

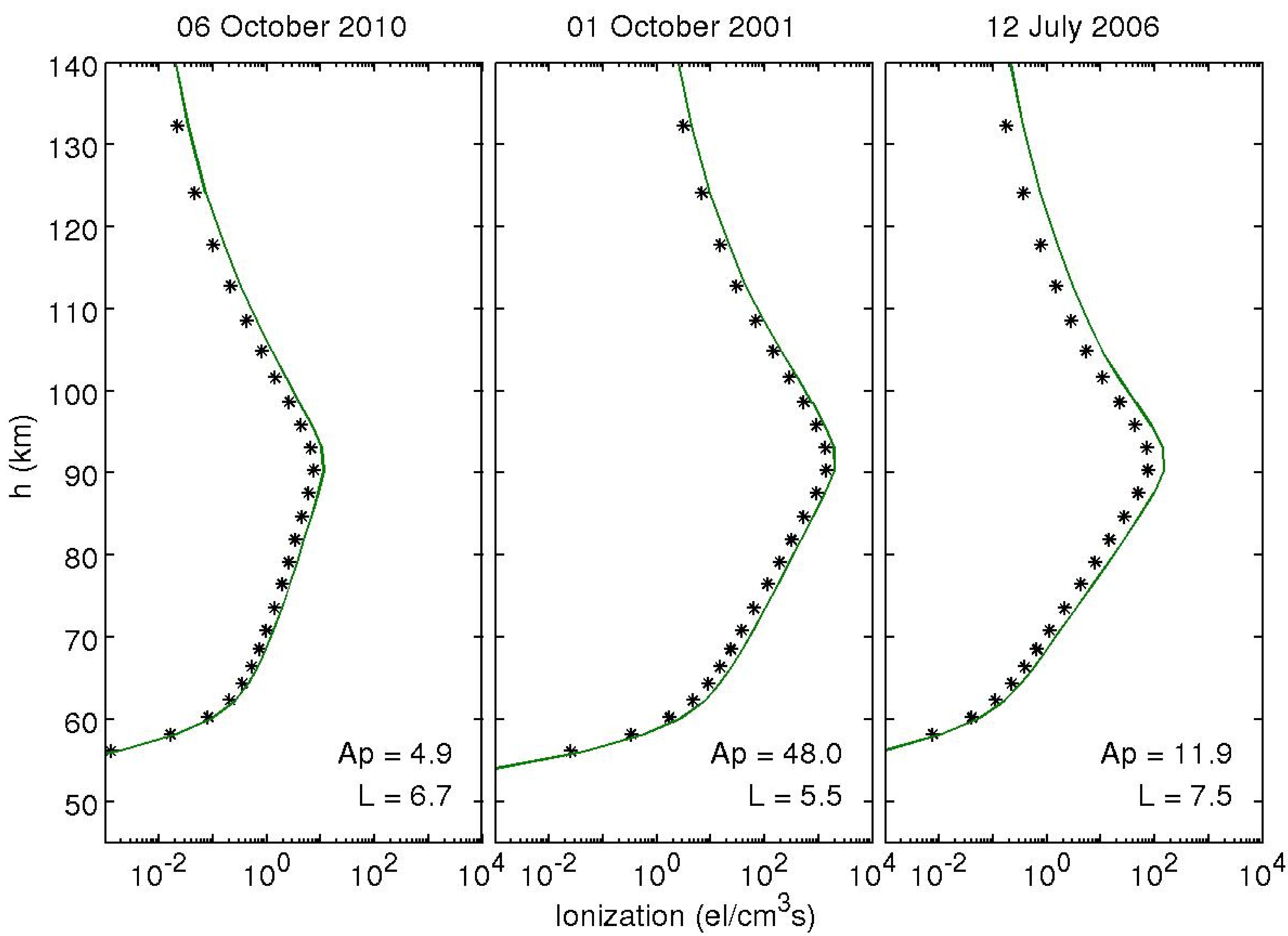
06 October 2010
01 October 2001
12 July 2006
h (km)
140
130
120
110
100
90
80
70
60
50
Ap = 4.9
L = 6.7
Ap = 48.0
L = 5.5
Ap = 11.9
L = 7.5
10^{-2}
10^{0}
10^{2}
10^{4}
Ionization (el/cm^{3}s)

Figure 11.

06 October 2010
01 October 2001
12 July 2006
h = 90 km
h = 76 km
h = 62 km
Ap = 4.9
L = 6.7
Ap = 48.0
L = 5.5
Ap = 11.9
L = 7.5
Ionization (el/cm^{3}s)
MLT (hr)
MLT (hr)
MLT (hr)

Figure 12.

Median ∈ F30
Median ∈ F30 (log10 of el/cm2s sr)
Spread ∈ F30
Spread of ∈ F30 (log10 of el/cm2s sr)
Median ∈ F300
Median ∈ F300 (log10 of el/cm2s sr)
Spread ∈ F300
Spread of ∈ F300 (log10 of el/cm2s sr)
L shell
Ap

Figure 13.


Median ϵ_{F30}
Spread ϵ_{F30}
Median ϵ_{F300}
Spread ϵ_{F300}
L shell
Ap
Median ϵ_{F30} ($\log_{10}$ of el/cm^{2}s sr)
Spread of ϵ_{F30} ($\log_{10}$ of el/cm^{2}s sr)
Median ϵ_{F300} ($\log_{10}$ of el/cm^{2}s sr)
Spread of ϵ_{F300} ($\log_{10}$ of el/cm^{2}s sr)

Figure 14.

Modelled electron flux > 30keV
L shell
Ap
Median F_{30} ($\log_{10}$ of el/cm^{2}s sr)
2
3
5
10
20
30
50
100
Modelled spectral gradient
L shell
Ap
Median k
-1
-2
-3
-4
-5

Figure 15.

$\log_{10}S(E)$ (2016) - $\log_{10}S(E)$ (2018)
L shell
E = 30 keV
E = 100 keV
E = 300 keV
Ap
Difference ($\log_{10}$ of el/cm^{2}s sr keV)